Cadmium Carboxylate Preparation Method Impacts the Synthesis of CdSe Nanoplatelets through Differences in Dissolution Kinetics

Benoit Wagnon, Rodolphe Valleix, Benjamin Abécassis

Cadmium carboxylate preparation method impacts the synthesis of CdSe Nanoplatelets through differences in dissolution kinetics

Benoit Wagnon,[1,*] Rodolphe Valleix,[1,*] and Benjamin Abécassis[1,†]

[1] *CNRS, ENS de Lyon, LCH, UMR 5182, 69342, Lyon cedex 07, France*

(Dated: April 25, 2025)

Colloidal CdSe nanoplatelets (NPL) are promising materials for various applications due to their unique optical properties arising from their atomically controlled thickness. However, the lack of understanding of their formation mechanism can result in low yields, multiple side products that are hard to separate, and unknown ligand composition at their surface. All these factors hinder the development and exploitation of such nanocrystals in devices. Herein, we focused on assessing the effect of long-chain cadmium(II) carboxylates (oleate and myristate) preparation methods on NPL synthesis. While cadmium(II) myristate always crystallizes in a lamellar structure irrespective of its preparation pathway, we show that cadmium(II) oleate displays two structures, one amorphous and one lamellar, that coexist in different relative concentrations depending on the synthesis method used to prepare the precursor. These differences impact the NPL synthesis through the precursor dissolution rate, which varies according to its supramolecular structure. The lamellar structure dissolves faster and yields thinner NPL than the amorphous one.

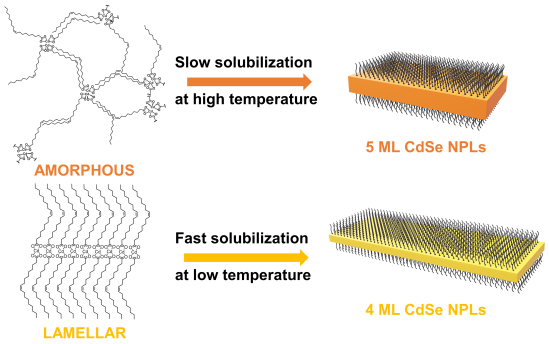

I. INTRODUCTION

Since the early 1980s and triggered by the pioneering work of Murray *et al.* [1], colloidal semiconductor nanocrystals have garnered a large interest of the scientific community. Among colloidal nanocrystals, nanoplatelets are semiconductor nanoparticles, typically II-VI materials such as CdE [2–5], or ZnE [6–8] (E = S, Se or Te), with one dimension much smaller than the two others. Their main advantage is their thickness-tunable optical properties, producing bright luminescence that holds promise for applications ranging from low-fluency energy threshold lasers to down-conversion for displays and lighting [9–11]. Synthesis of zinc-blende CdSe nanoplatelets (NPLs) involves the use of long hydrocarbon chains cadmium(II) carboxylates ($Cd(O_2CR)_2$) that ensure colloidal stability. Riedinger *et al.* demonstrated synthesizing CdSe NPLs in melt, without solvent and molecular template [12]. According to the authors, the generation of $(CdSe)_i$ monomers occurs through the reaction between *in situ* generated bis-(acyl)selenide and cadmium carboxylate [13]. In this case, NPLs form in a highly concentrated precursor environment, which is also likely to be the case for the standard syntheses octadecene since phase separation induced by the injection of $Cd(OAc)_2$ leads to high local concentration. Peng *et al.* proposed an oriented attachment-based mechanism the same year [14]. In this interpretation, symmetry breaking occurs early in the synthesis by forming flat QDs intermediates, which then undergo intraparticle ripening. However, this mechanism has been ruled out in two *in situ* X ray scattering studies. In one of them, Castro *et al.* applied a heating ramp to the cadmium oleate and acetate mixture corresponding to their final ratio [15]. They do not observe the formation of either a lamellar phase or small nanocrystals. In another study, van der Bok *et al.* show the presence of small spherical nanocrystals but their number increases or stays constant over time, in contradiction with ripening [16].

Techniques such as size-selective precipitation have been developed to obtain samples with high thickness purity, but they cause a decrease in the overall chemical yield. In this regard, the choice of precursors and how they influence the synthesis is particularly interesting. Much effort has been devoted to studying the influence of the selenium precursor on the outcome of 3 and 4 monolayers (ML) NPLs synthesis [13, 17]. Additionally, the influence of several experimental parameters such as temperature, reaction time, and presence of water have been presented as ways to control the outcome of CdSe NPLs synthesis [18]. When no water nor hydroxide anions are added to the reaction medium, the aspect ratio of 4 ML NPLs increases, which points towards the role of hydroxide anions in promoting width growth. Furthermore, lateral dimensions can be controlled through seeded-growth synthesis [19]. To the best of our knowledge, studies on the influence of the nature of the cadmium(II) precursor remain scarce [20, 21]. However, they

* These two authors contributed equally
† To whom correspondence should be addressed: benjamin.abecassis@ens-lyon.fr

dramatically influence the synthesis behavior. Indeed, the two primary cadmium sources employed in the literature are cadmium(II) oleate ($Cd(oleate)_2$) and myristate ($Cd(myr)_2$) [22, 23]. Moving from one to another yields 5 ML or 4 ML CdSe NPL as major products. In ref [24], we showed that CdSe NPLs can be synthesized using a single cadmium carboxylate baring a C8 chain. However, the effect of the precursor synthesis protocol on NPL synthesis outcome remains understudied. García-Rodrígez *et al.* [25] showed that in apolar solvents such as toluene, cadmium carboxylates exist as coordination polymers consisting of 30 molecular units whose precise structure likely impact the synthesis behavior, begging for further investigations.

$Cd(O_2CR)_2$ can be prepared through different pathways, yielding several impurities such as oxides and hydroxides alongside the desired product [26, 27]. Some syntheses involve the co-precipitation of salts (*e.g.*, $NaNO_3$ - Scheme 1), which can remain present as impurities despite extensive washing procedures[26]. In 2015, Hendricks *et al.* proposed a strategy to avoid the presence of water and hydroxide during the formation of the lead(II) carboxylates [28]. This method allows the preparation of anhydrous $Cd(O_2CR)_2$ compounds with excellent yield (*c.a.*, 97%) and offers the possibility to identify possible impurities by solution ^{19}F NMR.

This article reports the assessment of the influence of $Cd(myr)_2$ and $Cd(oleate)_2$ preparation methods on the synthesis outcome of CdSe NPLs. We show that the preparation method of $Cd(myr)_2$ does not significantly impact the NPL's thickness, lateral dimensions, and relative populations. In contrast, important differences are observed for $Cd(oleate)_2$. In particular, no 5 ML are obtained when $Cd(oleate)_2$ prepared from Hendricks' method is used. Instead, a mixture of smaller thicknesses is produced. After an in-depth study of each precursor using Fourier Transform Infrared Spectroscopy (FT-IR), ThermoGravimetric Analysis (TGA), powder X-Ray Diffraction (XRD), and Small Angle X-ray Scattering (SAXS), we attribute these variations to the precursor's supramolecular organization which impacts its dissolution kinetics rather than to impurities.

II. RESULTS AND DISCUSSION

Cadmium(II) carboxylates were synthesized according to procedures described in scheme 1 with slight modifications compared to the literature (detailed protocols are available in the supporting information). $Cd(O_2CR)_2$ precursors obtained through the nitrate route (scheme 1) and through the trifluoroacetate route (scheme 1) will be referred to as "A" and "B", respectively. The nitrate route involves the addition of $Cd(NO_3)_2.4H_2O$ dissolved in methanol in a solution of the corresponding sodium carboxylates in methanol, causing the $Cd(O_2CR)_2$ to precipitate. For the trifluoroacetate route (Scheme 1),

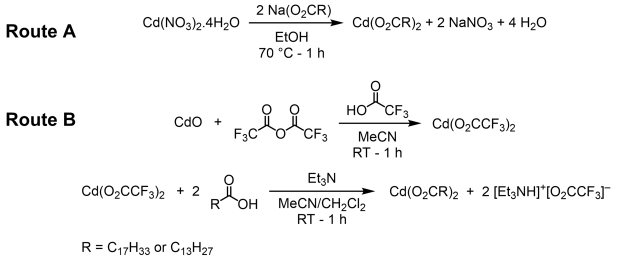

FIG. 1. Reactions yielding $Cd(O_2CR)_2$ following the nitrate (route A) and the trifluoroacetate (route B).

the desired cadmium(II) carboxylate is first obtained by the *in situ* generation of cadmium(II) trifluoroacetate. Then, the fatty acid is added to triethylamine, allowing the precipitation of cadmium(II) carboxylates and the formation of side-products such as triethylammonium trifluoroacetate ($[Et_3NH]^+[CF_3CO_2]^-$, scheme 1). In all the cases, products were washed thoroughly (with excess MeOH and acetonitrile/diethyl ether for route A or B, respectively) before being used to synthesize CdSe NPL.

The first set of conditions (*i.e.*, **protocol 1**) involves precursor A (see ESI for experimental details) [2]. Starting from $Cd(oleate)_2$ A yields 5.5 monolayers (5ML) CdSe nanoplatelets as evidenced by a heavy-hole/electron (λ_{hh-e}) transition centered at 550 nm (Figure 2A) and emission centered at 554 nm (Figure S5A). They are the main product of the reaction according to the strong resemblance between the crude and the purified NPLs UV-Vis absorption spectra. During purification, we separated quantum dots with λ_{hh-e} = 530 nm (diameter of $\simeq$3.5 nm [29]), responsible for the slight broadening of the 554 nm emission peak of the crude compared to the purified 5 ML NPL emission (Figure S5A). TEM analysis confirmed the quantum dots diameter (Figure S6) as well as the quasi-rectangular shape (Figure 2B and D) of the 5 ML NPLs with a lateral dimension of 23.0 nm × 9.9 nm (length (l) × width (w)).

In the second set of conditions (*i.e.*, **protocol 2**), $Cd(oleate)_2$ B from the trifluoroacetate route was used with great attention given to removing water from the reaction medium: all solvents (including hexane and 1-octadecene) were dried over CaH_2, distilled, and stored on molecular sieves in an Ar-filled glovebox (0 ppm of water measured through Karl-Fisher analysis - see ESI). Reagents and dry solvent were loaded in a round-bottom flask inside a glovebox. Moreover, cadmium acetate was loaded in a powder addition funnel to ensure perfectly air-free manipulation. The synthesis was then performed on a Schlenk line using standard air-free techniques, and nanocrystals were exposed to the ambient atmosphere only during purification steps. The outcome of the synthesis drastically differs from the first set of experimental conditions: a mixture of several nanocrystals is obtained: a majority of rectangular (aspect ratio of 4.4) 4 ML NPL

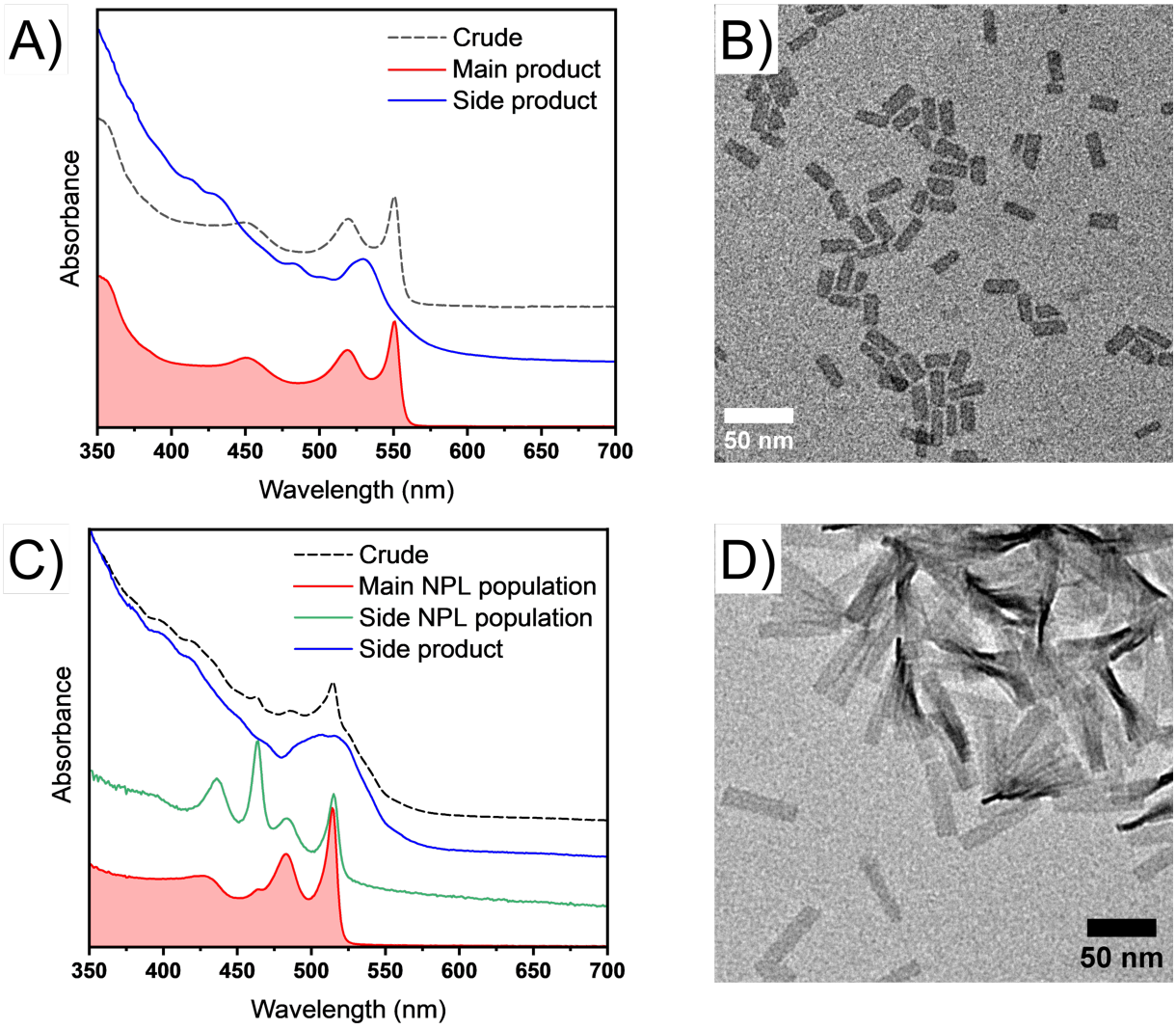

FIG. 2. UV-Vis spectra and TEM image of the main nanocrystals populations obtained after NPL synthesis with $Cd(oleate)_2$ A following protocol from the literature [2] (A - red trace and B) and with precursor B under strictly anhydrous and anaerobic conditions (C - red trace and D). Additionally, in A and C, one can see UV-Vis spectra of crude mixtures (dashed lines), isolated side products (*i.e.*, quantum dots - blue) and NPL side population (green).

(λ_{hh-e} = 514 nm) with 3 ML NPL (λ_{hh-e} = 462 nm) and quantum dots as side products, instead of almost pure 5 ML NPL (Figures 2B and S5C). From the broad quantum dot absorption, one can deduce that it consists of at least two populations with maxima centered at 503 nm and 517 nm (diameter of ∼3.1 nm and ∼3.3 nm, respectively). The increased aspect ratio without water nor hydroxide anions is consistent with Bertrand *et al.* [18].

Owing to their large lateral dimension ($l \times w$ = 59.4 × 13.4 nm^2), these 4 ML NPLs twist in a helicoidal shape (Figure 2D). This shape is obtained when the [110] crystallographic axis parallels their long edge [30, 31]. Moreover, their large lateral dimensions explain why they do not separate from 3 ML NPL upon size-selective precipitation and their lack of colloidal stability in hexane. This is consistent with a Bragg peak at q^*= 0.119 $Å^{-1}$ (5.3 nm) related to two nanoplatelets separated by interdigitated oleate hydrocarbon chain observed by SAXS (Figure S5D). This behavior differs from the usual stable suspension in alkane solvent, such as the one demonstrated by 5 ML NPL, which shows no precipitation nor stacking peak upon storage. Interestingly, this synthesis affords 4ML NPL with a mixture of oleate and acetate ligands at their surface, while previous protocols involved 3 cadmium(II) carboxylate (acetate, myristate, and oleate produced by injection of oleic acid at the end of the synthesis), which are expected to form the NPL ligand shell. Hence, these experiments allow better control over the ligand's composition and a simplified surface chemistry.

We carried out syntheses following the same experi-

mental conditions (*i.e.*, **protocol 1** and **2**) but using cadmium(II) myristate ($Cd(myr)_2$) A and B instead of the corresponding $Cd(oleate)_2$ (Figures S7 and S8). There was no drastic change between the two experimental conditions: 3 and 4 ML nanoplatelets emitting at 462 nm and 514 nm (Figures S7B and S8B), and quantum dots were obtained in both cases. Using $Cd(myr)_2$ B induces: 1) a broadening of the quantum dot emission, indicating a higher degree of polydispersity, and 2) the disappearance of the small 5 ML NPL population with $\lambda_{hh-e} = 543$ nm (Figures S7A and S8A). In addition, this change in experimental conditions induces an increase in the aspect ratio of the rectangular 4 ML NPL from 1.1 ($l \times w = 18.3 \times 16.4$ nm^2) (Figure S10A) to 4.0 ($l \times w = 32.9 \times 8.2$ nm^2) (Figure S9A), similar to what Bertrand *et al.* previously reported [18]. Interestingly, no twisting is observed in the latter case, even though the aspect ratio is close to the 4 ML NPL obtained previously with $Cd(oleate)_2$ B. This can be explained in two ways. First, both NPL samples can have the same curvature, but only the larger NPLs bend enough for the twist to be detected by electronic microscopy. Second, the presence of a myristate chain at the NPL surface could reduce the strain exerted by the ligand shell on the crystal structure, leading to a flat NPL [30].

We performed control experiments to understand if the differences in the synthesis behavior stem from the cadmium(II) salts or the presence of water and oxygen from the solvents. To do so, $Cd(myr)_2$ B and $Cd(oleate)_2$ B were employed, but solvents were used as received without further purification. No significant changes were observed (Figures S11 and S12) except for the lower amount of 3 ML NPL for solvent without purification (Figure S12). Even though water should alter the NPL surface ligand coverage, its presence does not influence the 4 ML NPLs curvature, showing that surface chemistry is not the dominant factor for NPL bending. This supports the hypothesis that NPL twisting is primarily due to their large lateral dimension rather than bound myristate. Overall, we attributed all the above differences to the nature of the $Cd(O_2CR)_2$ salt employed and the synthetic route used.

We thus hypothesized that the differences in synthesis outcome are due to structural differences between the precursors prepared by different routes. The four different cadmium(II) salts were studied using FT-IR, TGA, and SAXS. FT-IR spectra for compound A display a very weak broad signal (3300 - 3400 cm^{-1}) corresponding to the stretching mode of water. This signal is absent from the $Cd(O_2CR)_2$ compound B (Figures S13A-C). It has been previously discussed that the quantity of water used to synthesize CdSe NPLs influences their lateral dimensions [18]. Thus, an uncontrolled amount of water such as in $Cd(O_2CR)_2$ A is likely to yield non-reproducible syntheses (this point will be later detailed). However, water is absent from the FT-IR spectra of carboxylates B (Figures 3 and S13A and C). Since trifluoroacetic acid is involved in the trifluoroacetate route, CF_3COOH will likely be present in the final product. However, the presence of trifluoroacetate moieties can be ruled out using a correlation between ^{19}F NMR and FT-IR spectroscopy (Figures S14A and S16). To estimate a higher bound for impurity concentration, we recorded ^{1}H and ^{19}F NMR spectra of TFA solutions at 0.001 to 1 mM with the same acquisition parameters (Figure S15). Even at 0.001 mM, a clear signal with a high signal to noise ratio is detected for the two nuclei. This proves that our samples have trace impurities below 0.005 % (molar) in TFA. In a more general way, the presence of free acids (oleic, myristic and trifluororacetic acids) can be ruled out by looking at the NMR (^{1}H and ^{19}F - Figure S14) and FT-IR (1400 - 1700 cm^{-1} - Figures 3 and S16) analyses. Elemental analyses performed on the $Cd(O_2CR)_2$ A and B show that precursors have been obtained pure (Table III in the ESI). One can note that in the case of $Cd(oleate)_2$ A traces (< 0.4 mol %) of nitrogen are obtained, this is likely due to the presence of cadmium nitrate used in the synthesis. However, such traces are unlikely to cause the observed changes in the precursor's structure and reactivity differences.

The crystallinity of the long-chain precursors can be qualitatively assessed using FT-IR spectroscopy in their fingerprint region (*i.e.*, $>$ 1500 cm^{-1}). In the case of $Cd(oleate)_2$ (Figure 3C), FT-IR spectra strongly depend on the preparation method. Indeed, focusing on the 1400-1100 cm^{-1} region, $Cd(oleate)_2$ B exhibits a progression of narrow bands, ascribed to wagging (ω) and twisting (τ) vibration modes, that is characteristic of a crystalline packing of the carbon chains. Additionally, the presence of a well-defined rocking (δ) signal at 722 cm^{-1} and the absence of narrow bands in the 1400-1100 cm^{-1} region leads to the conclusion that $Cd(oleate)_2$ B is more crystalline than $Cd(oleate)_2$ A. Cadmium(II) myristate shows high crystallinity no matter the synthetic method employed (Figure 3D). Indeed, their FT-IR spectra bear the same characteristic of regularly spaced twisting/wagging vibrations and close rocking signals. It is well-known that the spacing between vibration bands is also sensitive to the molecule conformation. The experimental spacing between vibrations is 22.6 cm^{-1}, close to the calculated ($\Delta_\nu = 326/(m+1)$; m being the number of methylene, -CH_2-, units) value of 25.1 cm^{-1} which strengthens our conclusion on the crystallinity of the cadmium(II) myristate [32, 33]. Finally, the downshift in the symmetric ($\nu_s(CH_2)$) and asymmetric ($\nu_{as}(CH_2)$) methylene vibration mode confirms that crystallinity increases from $Cd(myr)_2$ A to B. The binding mode can be determined from the analysis of the C=O vibrations. A summary of the vibration frequencies and the differences between symmetric and asymmetric vibrations ($\Delta\nu$(C=O) = ν_{as} - ν_s) is provided in table I.

$\Delta\nu$ reported here are in line with previously reported values [34]. Thus, we conclude that the chelating mode in

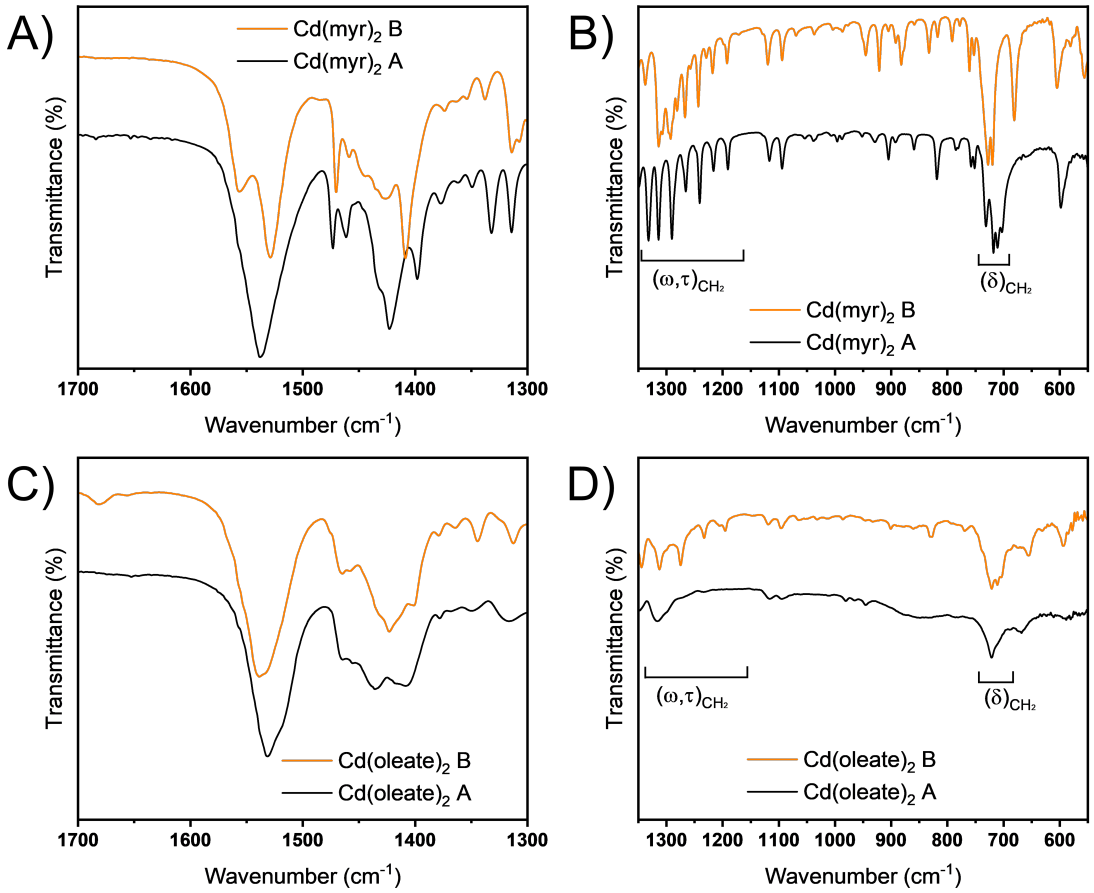

FIG. 3. FT-IR spectra of A), B) $Cd(oleate)_2$ and C), D) $Cd(myr)_2$ precursors.

Compounds	ν_{as}(C=O)	ν_s(C=O)	$\Delta\nu$(C=O)	ν_{as}(CH_2)	ν_s(CH_2)
$Cd(oleate)_2$ A	1531	1407	124	2920	2851
$Cd(oleate)_2$ B	1538	1401	137	2918	2850
$Cd(myr)_2$ A	1537	1398	139	2918	2849
$Cd(myr)_2$ B	1556	1408	148	2915	2847

TABLE I. Frequency values in the 1600-1400 cm^{-1} region and CH_2 vibration mode for $Na(CO_2R)$ and $Cd(CO_2R)_2$. All units are in cm^{-1} and full FT-IR spectra are presented on figures S16 and S17.

the primary binding mode in the cadmium(II) carboxylate compounds studied here.

Powder X-ray diffraction (Figure S18) confirms the interpretation of the FT-IR studies since $Cd(oleate)_2$ A displays no diffraction peak in contrast to $Cd(myr)_2$ samples. Interestingly, $Cd(myr)_2$ A displays weaker and slightly shifted peaks compared to $Cd(myr)_2$ B, a phenomenon explained by a lower degree of crystallinity of $Cd(myr)_2$ A.

Thermogravimetric analysis (TGA) was then performed under both air and inert atmosphere (nitrogen) with a slow heating rate (5 $K.min^{-1}$) to ensure that all the weight losses are observed. In air (Figures S19A and C), the overall weight losses are 78 % and 81 % in the case of $Cd(myr)_2$ B and A, respectively, in line with the following decomposition equation:

$$Cd(O_2CR)_2 \longrightarrow CdO + CO(g)CO_2(g)etc\cdot \qquad (1)$$

with R=$C_{13}H_{27}$ or $C_{17}H_{33}$. Moreover, X-ray diffraction analyses (Figures S19B and D) of post-TGA residues confirm the obtention of pure cadmium(II) oxide. Notably, cadmium(II) oxide formation occurs independently of the route to prepare the carboxylates. The same conclusions hold for the study of the oleates, where the overall losses are 80 % and 78 % for compounds A and B, respectively, agreeing with the expected value of 81 %.

The absence of a significant mass loss around 100 °C rules out the presence of water within the TGA detection limit, in line with FT-IR analysis.

TGA performed under an inert atmosphere (*i.e.*, nitrogen) strongly contrasts with the one obtained in air (Figure S20). The overall weight loss profile is close for A and B compounds. However, the total loss is higher in nitrogen. For example, the total loss is 90 % and 96 %

for $Cd(myr)_2$ B and $Cd(oleate)_2$ B, respectively. Following the work of Małecka *et al.*[35] on $Cd(formate)_2$, we assume that $CdCO_3$ and elemental Cd are plausible intermediates under an inert atmosphere. Thus, as the vapor pressure of the Cd_{metal} is increased at high temperature (∼9 kPa at 600 °C [35]), its sublimation is likely to occur, causing additional mass losses compared to analyses performed in air.

To further understand the structure of the Cd(II) precursors, we conducted SAXS analyses on the different $Cd(O_2CR)_2$ obtained *via* pathways A and B (Figure 4). For $Cd(myr)_2$ B (figures 4A and S21A), a series of peaks at $q^* = 0.170$ Å^{-1}, $2q^* = 0.340$ Å^{-1}, $3q^* = 0.510$ Å^{-1} appear in the SAXS diagram corresponding to a lamellar structure with a period of $d_{m1} = 3.70$ nm ($2\pi/q^*$). This value matches the theoretical distance between two Cd^{2+} centers assuming carbon chain interdigitation. Indeed, this value can be broken apart into two components: the metal-O_2C distance approximated to 0.275 nm (0.55 nm for two Cd^{2+} centers [36]); and the length of the C14 carbon chain: 3.84 nm according to the Tandford's formula [37]. This yields a 0.69 nm interdigitation of the carbon chains. For $Cd(myr)_2$ synthesized *via* pathway A, a second series of peaks is observed at $q^* = 0.157$ Å^{-1}, $2q^* = 0.304$ Å^{-1}, $3q^* = 0.461$ Å^{-1}. These values correspond to a period increase of 0.30 nm, close to the length of one water molecule (0.28 nm) [38] likely to be found near the charged cadmium cation.

In the case of $Cd(oleate)_2$ (Figure 4B and S21B), a lamellar structure with a period of $d_{O1} = 4.51$ nm (0.139 Å^{-1}) is also observed. Compared to myristate, the Bragg peaks are broader, and the structure is thus less crystalline. We estimate the interdigitation to be 0.05 nm, indicating that the unsaturation prevents ligand interpenetration. The peak at $q^* = 0.237$ Å^{-1} ($d_{O2} = 2.65$ nm) is more difficult to interpret. Although d_{O2} is close to what is expected for two cadmium separated by one oleate chain plus a water or hydroxide moiety, its presence in the $Cd(oleate)_2$ B, which is water-free, rules out this hypothesis. To assess if this scattering peak is due to the presence of water, we hydrated the cadmium precursors in a controlled fashion using a chamber with a known relative humidity (see section III in the ESI). We will refer to these precursors as hydrated $Cd(O_2CR)_2$ B (R = $C_{13}H_{27}$ or $C_{17}H_{35}$). These precursors have been characterized by FT-IR, TGA and SAXS (see ESI section III and figures S13 and S21). For myristate and oleate precursors, Bragg peaks corresponding to the lamellar structure shift towards lower q and align with the one of cadmium carboxylate A. This confirms the presence of either water or hydroxide close to the metal center in those precursors. However, no detectable changes are observed for the peak at $q^* = 0.237$ Å^{-1}. Water has, therefore, no effect on the corresponding structure and is not at the origin of its formation.

We also performed control experiments to check if the solvent used to wash the precursors affected their structure. To do so, we compared the SAXS patterns of the two $Cd(oleate)_2$ washed with MeCN and MeOH (Figure S23). Since the SAXS patterns are the same, we ruled out this hypothesis.

We hypothesize the formation of a 3D network of intermingled oleate aliphatic chains, interacting through their carbon-carbon double bond and their head groups *via* hydrogen bonds, to explain the presence of the $q^* = 0.237$ Å^{-1} peak as depicted in figure 5. Such polymeric hydrogen bond-linked aggregates are present in bulk aliphatic alcohols such as octanol [39] and short-chain carboxylic acids [40]. Partial segregation between polar and polar domains yield a scattering peak, sometimes coined "pre-peak" in the small angle regime. This hypothesis also rationalizes the lower crystallinity of $Cd(oleate)_2$ A as shown on the FT-IR spectra (1350 - 550 cm^{-1} - Figure 3D). This structure is predominant against the lamellar phase in this precursor, as evidenced by the high intensity of the d_{O2} scattering peak compared to the d_{O1} one. Thus, there is competition between these two structures for $Cd(oleate)_2$, which is not happening for $Cd(myr)_2$. This is likely due to the presence of the alkene, which decreases the propensity of the tail to crystallize. Using cadmium(II) nitrate then promotes the formation of the $Cd(oleate)_2$ 3D network.

The d_{O2} relative intensity decreases compared to d_{O1} observed in the hydrated $Cd(oleate)_2$ B is more likely due to aging than to the presence of water as shown by the SAXS pattern of "aged" samples of cadmium precursors A and B, which were left for several weeks in close vials on the lab bench (Figure S21). Interestingly, aged $Cd(oleate)_2$ A does not show any peak at $q^* = 0.237$ Å^{-1} indicating the disappearance of the hypothesized 3D network. As we observed that aged $Cd(oleate)_2$ A tends to produce a mixture of 3, 4, and 5 ML, we conclude that the presence of the 3D network is key to obtaining 5 ML NPL and that this structure is kinetically unstable in the presence of water. On the other hand, the lamellar structure is more stable as aged $Cd(myr)_2$ only presents signs of hydration. Hence, storing this precursor in a water-free environment is an adequate strategy to conserve its properties.

To gain a better insight into the processes at work during NPL synthesis depending on the carboxylate cadmium precursor, we studied the formation mechanism of colloidal QD in conditions close to the NPL synthesis using a Linkam hot stage mounted on a SAXS lab instrument. We recall that the 4 and 5 ML NPL synthesis is very close to the classical heat-up synthesis of quantum dots [41] which consists of the heating of long chain cadmium carboxylate in the presence of elemental selenium, except that, for NPL, cadmium acetate is injected during the heating ramp. The formation mechanism of quantum dots in these conditions was studied by our group. [42] In short, the cadmium precursor was mixed with 1-octadecene and selenium

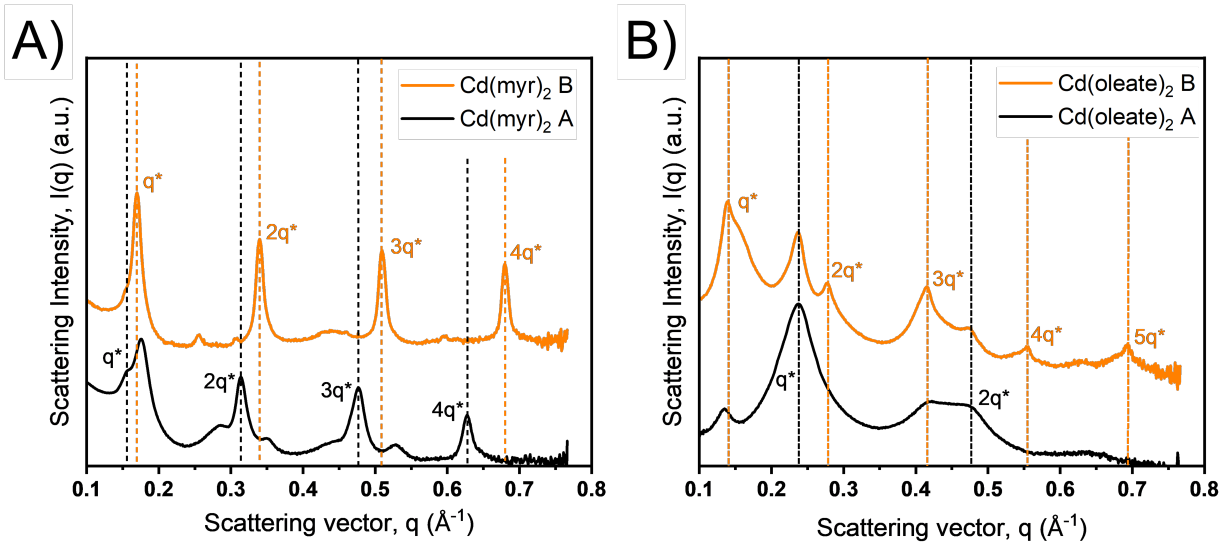

FIG. 4. SAXS pattern of A) $Cd(myr)_2$ and of B) $Cd(oleate)_2$ powders (B). Vertical dotted lines are added to help peak position comparison.

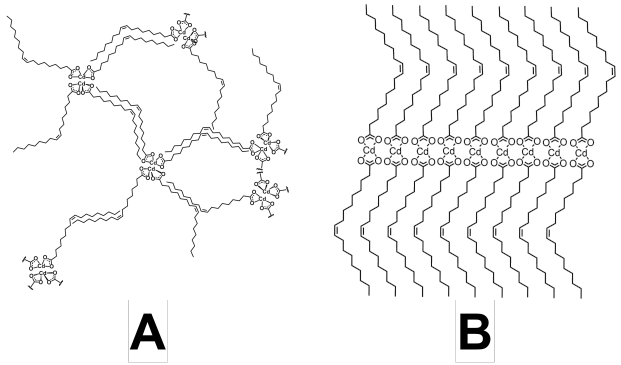

FIG. 5. Proposed schematic structures for amorphous and lamellar $Cd(O_2CR)_2$ precursors

powder. The mixture was sonicated and stirred for 10 min before introducing an aliquot into a SAXS glass capillary. The SAXS analysis was carried out from 30 °C to 240 °C and separated into two sequences. First, from 30 °C to 100 °C, one SAXS diagram is acquired every 5 °C. Then, from 100 °C to 240 °C, with a SAXS diagram every 10 °C. Annealing at 240 °C was also carried out for one hour with an acquisition every 5 min. The temperature rise was controlled so that two measures were separated by 1 min, and an equilibrium time of 30 s was implemented before each acquisition.

Figures 6A and B show the *in situ* SAXS results for $Cd(myr)_2$ A and B, respectively. At room temperature, we note Bragg peaks characteristic of a lamellar phase likely due to the low solubility of the $Cd(myr)_2$ in ODE. The temperature at which solubilization occurs depends on the synthesis route: 95 °C and 110 °C for $Cd(myr)_2$ A and B, respectively.

After solubilization of the cadmium precursors, the QD growth follows a similar trend as described previously. [43] We observe the formation of micelles with radii < 1 nm accompanied by an increase of the scattered intensity (I(q)) at $q^* > 0.2$ Å^{-1} and the $Cd(myr)_2$ precursor dissolution. Then, spherical nanoparticles appear, as highlighted by the increase of I(q) for $q^* > 0.2$ Å^{-1}. However, the temperatures of the onset of nucleation/growth processes differ compared to our previous study due to a slower temperature ramp: 170 °C and 160 °C form $Cd(myr)_2$ A and B, respectively, compared to 218.7 °C reported earlier [43] In this heating up process, QD growth is limited by the chemical formation of $(CdSe)_i$ monomer species. As $Cd(myr)_2$ dissolution occurs before that of selenium (recorded at 140 °C), monomer formation is limited by the generation of selenide reactive species such as H_2Se or bis(acyl) selenide.

In the case of $Cd(oleate)_2$ B (Figure 6D), the precursor dissolution is also fast. Low intensity Bragg peaks are still observed upon mixing the oleate precursor with 1-octadecene, but they are broadened compared to the powder form. We believe that the visible peak corresponds to the lamellar structure of $Cd(oleate)_2$ with disruption of the organized cadmium layer through the diffusion of 1-octadecene molecules in the crystalline network, causing the partial solubilization of the precursor. These peaks disappear at a low temperature (45 °C), indicating a fast solubilization of $Cd(oleate)_2$. Thus, the nucleation and growth pathway are the same as the one described for $Cd(myr)_2$.

In contrast, for $Cd(oleate)_2$ A (Figure 6C), the Bragg peak corresponding to the 3D network persists for temperatures above 100 °C. First, it is broadened and shifted

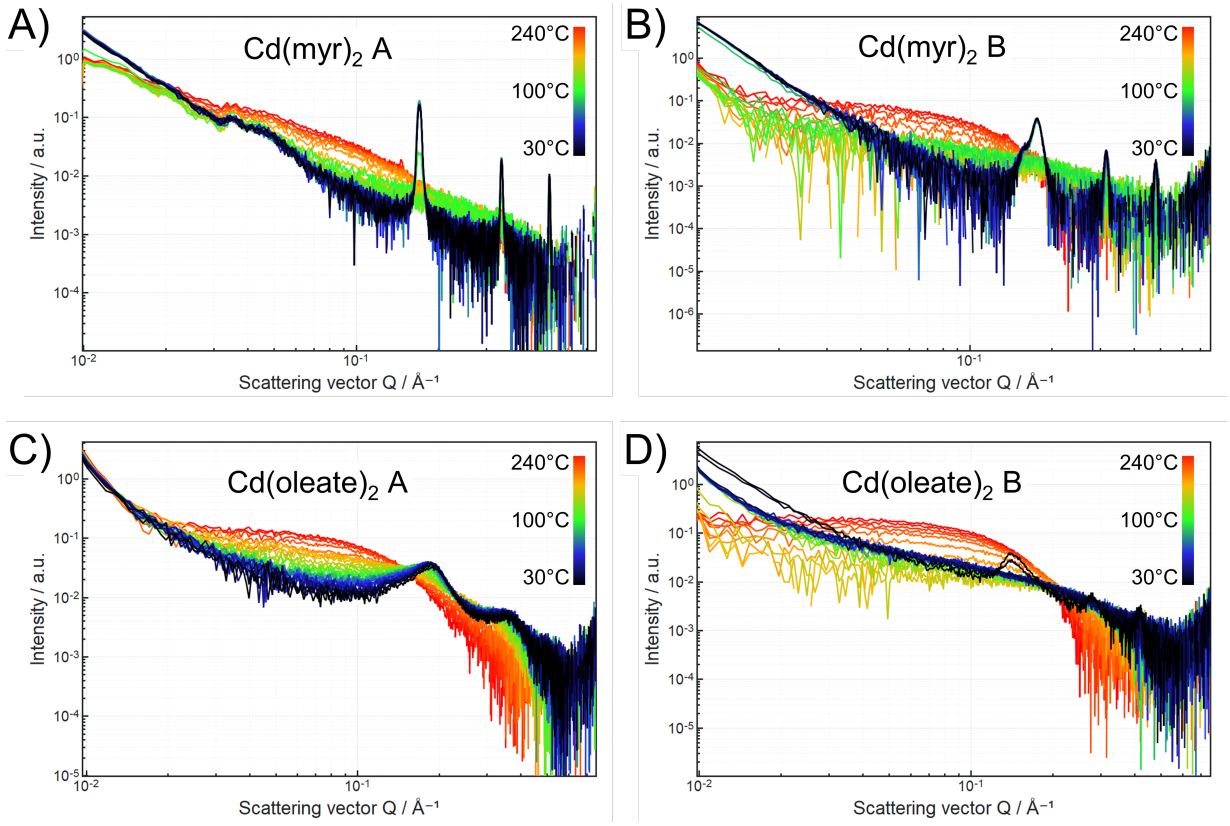

FIG. 6. SAXS pattern of the cadmium precursors dissolution and the growth of CdSe quantum dots for A) and B) $Cd(myr)_2$ A and B, respectively. C) and D) correspond to the SAXS pattern obtained for $Cd(oleate)_2$ A and B, respectively.

to 0.192 $Å^{-1}$ upon mixing with 1-octadecene at room temperature. Then, this shift further increases, and it gradually moves towards smaller q values (Δq^*= 0.042 $Å^{-1}$), which correspond to a distance expansion of Δd= 0.92 nm as the temperature rises, leading to the complete precursor dissolution at 170 °C. Hence, in this case, quantum dot nucleation/growth and precursor dissolution occur simultaneously. We hypothesize that this restriction in the cadmium availability leads to a lower seed concentration for the same amount of material, hence forming larger nanocrystals. This is confirmed by optical measurements of the QD solutions obtained obtained after our *in situ* experiments on $Cd(oleate)_2$ precursors. The absorption, emission, and excitation spectra of the QD are given in figures S22. The excitonic transitions are located at 528 nm and 521 nm for precursors A and B respectively. This corresponds to QD diameters of 2.9 and 2.7 nm. Interestingly, the difference between the diameters of the QDs obtained from $Cd(oleate)_2$ A and B correspond to the thickness of one CdSe layer, with $Cd(oleate)_2$ A giving the largest nanocrystals. These findings explain qualitatively why thicker NPL form with $Cd(oleate)_2$ A. The 2D growth is triggered by the injection of Cd(acetate) which occurs at around 200 °C. At this moment, larger nanocrystals are present in solution for precursor A since precursor dissolution is slower and less nuclei are present. Hence, the NPL nuclei (also coined mini-NPLs [16]) are thicker for precursor A and this thickness difference persists during NPL growth.

III. CONCLUSION

In conclusion, we showed that the synthesis pathway of cadmium carboxylate strongly impacts the synthesis of CdSe nanoplatelets, leading to different thickness populations. This effect was traced to structural differences between precursors at the supra-molecular level, which affect their solubilization kinetics during the synthesis process. For $Cd(oleate)_2$, the structure of the powder varies from a predominant amorphous network when the synthesis is performed from nitrate salt in methanol to a lamellar structure for anhydrous route (trifluoroacetic route). This leads, under the same experimental conditions, to the production of 59 × 13 nm^2 helicoidal 4 ML CdSe NPL instead of $(l \times w) = 23 \times 10$ nm^2 flat 5 ML CdSe NPL, respectively. By monitoring a heat-up quantum dot synthesis with these precursors, we found that the slow solubilization of this 3D network leads to the restricted availability of cadmium reactants to form nucleation centers. The limited amount of seeds for growth promotes large QD or mini-NPL, which leads to thicker

NPL. These findings highlight the importance of the synthesis pathway of metallic precursors on nanocrystal syntheses. These findings highlight the importance of the synthesis pathway of metallic precursors on nanocrystal syntheses. This opens the way to ligand and precursor design taking into account their dissolution kinetics. We believe this endeavor could be a path toward finding novel and robust protocols that yield pure and dimension-controlled NPLs. For example, we can hypothesize, based on the findings described here, that using a less soluble precursor could yield thicker NPL without using halide anions. [44, 45] In a broader perspective, the precursor supra-molecular organization and their solubility emerge as key factors warranting further investigation to gain insight in the formation mechanism of colloidal nanostructures.

ACKNOWLEDGMENTS

This article is part of a project that has received funding from the European Research Council (ERC) under the European Union's Horizon 2020 research and innovation program (Grant agreement No. 865995). This work was supported by the LABEX iMUST of the University of Lyon (ANR-10-LABX-0064), created within the program ≪Investissements d'Avenir≫ set up by the french government and managed by the French National Research Agency (ANR). The authors thank Dr. F. Chaput for his help in building the hygrometry-controlled setup, allowing us to obtain the hydrated precursors in a reproducible manner. Finally, the authors thank the CIQLE (Centre d'Imagerie Quantitative Lyon-Est) in Lyon for the availability of the transmission electron microscopy facility.

[1] C. B. Murray, D. J. Norris, and M. G. Bawendi, Synthesis and characterization of nearly monodisperse cde (e = sulfur, selenium, tellurium) semiconductor nanocrystallites, J. Am. Chem. Soc. **115**, 8706 (1993), https://doi.org/10.1021/ja00072a025.

[2] S. Ithurria and B. Dubertret, Quasi 2d colloidal cdse platelets with thicknesses controlled at the atomic level, J. Am. Chem. Soc. **130**, 16504 (2008), https://doi.org/10.1021/ja807724e.

[3] S. Ithurria, M. D. Tessier, B. Mahler, R. P. S. M. Lobo, B. Dubertret, and A. L. Efros, Colloidal nanoplatelets with two-dimensional electronic structure, Nat. Mater. **10**, 936–941 (2011).

[4] N. Saenz, L. S. Hamachi, A. Wolock, B. H. Goodge, A. Kuntzmann, B. Dubertret, I. Billinge, L. F. Kourkoutis, D. A. Muller, A. C. Crowther, and J. S. Owen, Synthesis of graded CdS1-xSex nanoplatelet alloys and heterostructures from pairs of chalcogenoureas with tailored conversion reactivity, Chemical Science **14**, 12345 (2023).

[5] A. Anand, M. L. Zaffalon, F. Cova, V. Pinchetti, A. H. Khan, F. Carulli, R. Brescia, F. Meinardi, I. Moreels, and S. Brovelli, Optical and scintillation properties of record-efficiency cdte nanoplatelets toward radiation detection applications, Nano Lett. **22**, 8900 (2022), https://doi.org/10.1021/acs.nanolett.2c02975.

[6] L. Dai, C. Strelow, T. Kipp, A. Mews, I. Benkenstein, D. Eifler, T. H. Vuong, J. Rabeah, J. McGettrick, R. Lesyuk, and C. Klinke, Colloidal manganese-doped zns nanoplatelets and their optical properties, Chem. Mater. **33**, 275 (2021), https://doi.org/10.1021/acs.chemmater.0c0375.

[7] P. D. Cunningham, I. Coropceanu, K. Mulloy, W. Cho, and D. V. Talapin, Quantized reaction pathways for solution synthesis of colloidal znse nanostructures: A connection between clusters, nanowires, and two-dimensional nanoplatelets, ACS Nano **14**, 3847 (2020), https://doi.org/10.1021/acsnano.9b09051.

[8] M. S. Es, E. Colak, A. Irfanoglu, and Y. Kelestemur, Direct synthesis of zinc-blende znse nanoplatelets, ACS Omega **9**, 27438 (2024), https://doi.org/10.1021/acsomega.4c02356.

[9] C. Dabard, H. Po, N. Fu, L. Makke, H. Lehouelleur, L. Curti, X. Z. Xu, E. Lhuillier, B. T. Diroll, and S. Ithurria, Expanding the color palette of bicolor-emitting nanocrystals, Nanoscale **15**, 14651 (2023).

[10] B. Guzelturk, Y. Kelestemur, M. Olutas, S. Delikanli, and H. V. Demir, Amplified spontaneous emission and lasing in colloidal nanoplatelets, ACS Nano **8**, 6599 (2014), https://doi.org/10.1021/nn5022296.

[11] B. T. Diroll, B. Guzelturk, H. Po, C. Dabard, N. Fu, L. Makke, E. Lhuillier, and S. Ithurria, 2d ii–vi semiconductor nanoplatelets: From material synthesis to optoelectronic integration, Chem. Rev. **123**, 3543 (2023), https://doi.org/10.1021/acs.chemrev.2c00436.

[12] A. Riedinger, F. D. Ott, A. Mule, S. Mazzotti, P. N. Knüsel, S. J. P. Kress, F. Prins, S. C. Erwin, and D. J. Norris, An intrinsic growth instability in isotropic materials leads to quasi-two-dimensional nanoplatelets, Nat Mater **16**, 743 (2017).

[13] A. Riedinger, A. S. Mule, P. N. Knüsel, F. D. Ott, A. A. Rossinelli, and D. J. Norris, Identifying reactive organo-selenium precursors in the synthesis of cdse nanoplatelets, Chem. Commun. **54**, 11789 (2018).

[14] Y. Chen, D. Chen, Z. Li, and X. Peng, Symmetry-breaking for formation of rectangular cdse two-dimensional nanocrystals in zinc-blende structure, J. Am. Chem. Soc. **139**, 10009 (2017), https://doi.org/10.1021/jacs.7b04855.

[15] N. Castro, C. Bouet, S. Ithurria, N. Lequeux, D. Constantin, P. Levitz, D. Pontoni, and B. Abécassis, Insights into the Formation Mechanism of CdSe Nanoplatelets Using in Situ X-ray Scattering, Nano Lett. **19**, 6466 (2019).

[16] J. C. van der Bok, P. T. Prins, F. Montanarella, D. N. Maaskant, F. A. Brzesowsky, M. M. van der Sluijs, B. B. V. Salzmann, F. T. Rabouw, A. V. Petukhov, C. De Mello Donega, D. Vanmaekelbergh, and A. Meijerink, *In Situ* Optical and X-ray Spectroscopy Reveals Evolution toward Mature CdSe Nanoplatelets by Synergetic Action of Myristate and Acetate Ligands, J. Am. Chem. Soc. **144**, 8096 (2022).

[17] A. Di Giacomo, A. Myslovska, V. De Roo, J. Goeman, J. C. Martins, and I. Moreels, Selenium reduction pathways in the colloidal synthesis of cdse nanoplatelets, Nanoscale **16**, 6268 (2024).

[18] G. H. V. Bertrand, A. Polovitsyn, S. Christodoulou, A. H. Khan, and I. Moreels, Shape control of zincblende CdSe nanoplatelets, Chem. Commun. **52**, 11975 (2016).

[19] C. Bouet, B. Mahler, B. Nadal, B. Abecassis, M. D. Tessier, S. Ithurria, X. Xu, and B. Dubertret, Two-Dimensional Growth of CdSe Nanocrystals, from Nanoplatelets to Nanosheets, Chem. Mater. **25**, 639 (2013).

[20] Y. Jiang, W.-S. Ojo, B. Mahler, X. Xu, B. Abécassis, and B. Dubertret, Synthesis of cdse nanoplatelets without short-chain ligands: Implication for their growth mechanisms, ACS Omega **3**, 6199–6205 (2018).

[21] A. Di Giacomo, C. Rodà, A. H. Khan, and I. Moreels, Colloidal synthesis of laterally confined blue-emitting 3.5 monolayer cdse nanoplatelets, Chemistry of Materials **32**, 9260–9267 (2020).

[22] S. Ithurria and B. Dubertret, Quasi 2D Colloidal CdSe Platelets with Thicknesses Controlled at the Atomic Level, J. Am. Chem. Soc. **130**, 16504 (2008).

[23] S. Jana, M. de Frutos, P. Davidson, and B. Abécassis, Ligand-induced twisting of nanoplatelets and their self-assembly into chiral ribbons, Sci. Adv. **3**, e1701483 (2017).

[24] Y. Jiang, W.-S. Ojo, B. Mahler, X. Xu, B. Abécassis, and B. Dubertret, Synthesis of CdSe Nanoplatelets without Short-Chain Ligands: Implication for Their Growth Mechanisms, ACS Omega **3**, 6199 (2018).

[25] R. García-Rodríguez and H. Liu, Solution structure of cadmium carboxylate and its implications for the synthesis of cadmium chalcogenide nanocrystals, Chemical Communications **49**, 7857 (2013).

[26] R. García-Rodríguez, M. P. Hendricks, B. M. Cossairt, H. Liu, and J. S. Owen, Conversion Reactions of Cadmium Chalcogenide Nanocrystal Precursors, Chem. Mater. **25**, 1233 (2013).

[27] N. Pilpel, Properties of Organic Solutions of Heavy Metal Soaps., Chemical Reviews **63**, 221 (1963).

[28] M. P. Hendricks, M. P. Campos, G. T. Cleveland, I. J.-L. Plante, and J. S. Owen, A tunable library of substituted thiourea precursors to metal sulfide nanocrystals, Science **348**, 1226 (2015), https://www.science.org/doi/pdf/10.1126/science.aaa2951.

[29] T. Aubert, A. A. Golovatenko, M. Samoli, L. Lermusiaux, T. Zinn, B. Abécassis, A. V. Rodina, and Z. Hens, General Expression for the Size-Dependent Optical Properties of Quantum Dots, Nano Lett. **22**, 1778 (2022).

[30] D. Monego, S. Dutta, D. Grossman, M. Krapez, P. Bauer, A. Hubley, J. Margueritat, B. Mahler, A. Widmer-Cooper, and B. Abécassis, Ligand-induced incompatible curvatures control ultrathin nanoplatelet polymorphism and chirality, PNAS **121**, 10.1073/pnas.2316299121 (2024).

[31] C. Bouet, M. D. Tessier, S. Ithurria, B. Mahler, B. Nadal, and B. Dubertret, Flat Colloidal Semiconductor Nanoplatelets, Chem. Mater. **25**, 1262 (2013).

[32] A. Antanovich, A. Prudnikau, A. Matsukovich, A. Achtstein, and M. Artemyev, Self-Assembly of CdSe Nanoplatelets into Stacks of Controlled Size Induced by Ligand Exchange, J. Phys. Chem. C **120**, 5764 (2016).

[33] I. Levine, S. M. Weber, Y. Feldman, T. Bendikov, H. Cohen, D. Cahen, and A. Vilan, Molecular length, monolayer density, and charge transport: Lessons from al–alox/alkyl–phosphonate/hg junctions, Langmuir **28**, 404 (2012), https://doi.org/10.1021/la2035664.

[34] M. Mesubi, An infrared study of zinc, cadmium, and lead salts of some fatty acids, Journal of Molecular Structure **81**, 61 (1982).

[35] B. Malecka and A. Lacz, Thermal decomposition of cadmium formate in inert and oxidative atmosphere, Thermochimica Acta **479**, 12–16 (2008).

[36] M. Guenane, C. Forano, and J. P. Besse, Intercalation of organic pillars in [Zn-Al] and [Zn-Cr] layered double hydroxides, Mater. Sci. For. **152-153**, 343 (1994).

[37] C. Tanford, Micelle shape and size, J. Phys. Chem. **76**, 3020 (1972).

[38] J. S. D'Arrigo, Screening of membrane surface charges by divalent cations: an atomic representation, Am. J. Physiol. Cell Physiol. **235**, C109 (1978).

[39] S. E. DeBolt and P. A. Kollman, Investigation of Structure, Dynamics, and Solvation in 1-Octanol and Its Water-Saturated Solution: Molecular Dynamics and Free-Energy Perturbation Studies, Journal of the American Chemical Society **117**, 5316 (1995).

[40] A. Mariani, A. Innocenti, A. Varzi, and S. Passerini, On the nanoscopic structural heterogeneity of liquid n-alkyl carboxylic acids, Physical Chemistry Chemical Physics **23**, 20282 (2021).

[41] Y. A. Yang, H. Wu, K. R. Williams, and Y. C. Cao, Synthesis of CdSe and CdTe Nanocrystals without Precursor Injection, Angewandte Chemie International Edition **44**, 6712 (2005).

[42] B. Abécassis, C. Bouet, C. Garnero, D. Constantin, N. Lequeux, S. Ithurria, B. Dubertret, B. R. Pauw, and D. Pontoni, Real-Time in Situ Probing of High-Temperature Quantum Dots Solution Synthesis, Nano Lett. **15**, 2620 (2015).

[43] B. Abécassis, C. Bouet, C. Garnero, D. Constantin, N. Lequeux, S. Ithurria, B. Dubertret, B. R. Pauw, and D. Pontoni, Real-time in situ probing of high-temperature quantum dots solution synthesis, Nano Lett. **15**, 2620 (2015), https://doi.org/10.1021/acs.nanolett.5b00199.

[44] W. Cho, S. Kim, I. Coropceanu, V. Srivastava, B. T. Diroll, A. Hazarika, I. Fedin, G. Galli, R. D. Schaller, and D. V. Talapin, Direct Synthesis of Six-Monolayer (1.9 nm) Thick Zinc-Blende CdSe Nanoplatelets Emitting at 585 nm, Chem. Mater. **30**, 6957 (2018).

[45] S. Christodoulou, J. I. Climente, J. Planelles, R. Brescia, M. Prato, B. Martín-García, A. H. Khan, and I. Moreels, Chloride-Induced Thickness Control in CdSe

Nanoplatelets, Nano Lett. **18**, 6248 (2018).

[46] Y. Marcus, Volumes of aqueous hydrogen and hydroxide ions at 0 to 200 °C, J. Chem. Phys. **137**, 154501 (2012)

SUPPLEMENTARY MATERIAL

IV. MATERIALS AND METHODS

Reagents. Sodium oleate (82 %), myristic acid (98%), ethanol (96 %), absolute ethanol, isopropanol (99%), methanol (99 %), selenium powder (99.5 %), cadmium acetate dihydrate (98 %), oleic acid (99%) and oleic acid (90 %) were purchased from Sigma-Aldrich. 1-octadecene (ODE, 90 %) and hexane (90 %), were supplied by Fisher-Agros Organics. Ethyl acetate (99 %) and cadmium nitrate tetrahydrate (98.5 %) were supplied by Fisher-Alfa Aesar. Sodium myristate (98%) was bought from TCI. $CDCl_3$ was purchased form Eurisotop. When anhydrous solvents were required, they were dried over CaH_2 under strong stirring overnight before their distillation. Solvents are then stored in glovebox over 4 Å molecular sieves for further use.

UV-Vis spectroscopy was performed using a JASCO V-730 spectrophotometer. The suspension were prepared by diluting 15 μL of the sample in 2 mL hexane in quartz cuvette prior any measurement.

Fluorescence spectroscopy studies have been performed using a PerkinElmer FL-8500 fluorimeter. The same sample preparation as for the UV-Vis measurements was used to measure fluorescence spectra

Fourier transform infrared spectroscopy (FT-IR) analyses were carried out on Perkin-Elmer Spectrum 65 spectrometer in attenuated total reflection (ATR) mode on the precursor powders in air. Several measures were carried out on compounds B to ensure their air stability and the reliability of our measurements.

Thermogravimetric analyses (TGA) were carried out using on a Setaram Labsys Evo TG DTADSC+ 1600 °C under either air or N_2 atmosphere. Samples of about 20 mg were weighed in 100 μL aluminum oxide crucibles. Prior to measurements, the crucibles were pyrolized at 1200 °C and stored in a oven at 175 °C to ensure no water adsorption. Then, samples were heated from RT up to either 500 °C or 1000 °C with a heating rate of 5 $K.min^{-1}$.

Small Angle X-ray Scattering (SAXS) experiments were performed using a XENOCS Xeuss 3.0 SAXS instrument with a X-ray energy of 8 keV. Sample-to-detector distance was set to 350 mm and a sampling time of 300 s was used to measure scattering. Roughly 100 µL of the NPL solution was inserted in a glass capillaries with an overall diameter of 1.5 mm for measurement.

Transmission electron microscopy (TEM) images were acquired with a JEOL JEM-1400 electron microscope equipped with a 100-kV field emission gun at CIQLE Lyon. One drop of diluted samples was drop-casted on a copper/carbon 300 mesh TEM grids (Tedd Pella). Nanoplatelets suspension were diluted 10 times to enable a suitable observation.
HR-STEM pictures have been acquired with a Jeol Neoarm operating at 200 kV at the Centre Electronique de Microscopie Stéphanois, in Saint-Etienne (France).

Nuclear magnetic resonance (NMR) analyses were performed using a Bruker Advance 300 MHZ spectrometer equipped with a 5mm broadband direct probe BBFO 1H- X Z gradient.

Karl-fisher titration was used to estimate the water content in the employed solvents after drying and distillation, The measure were determined using a Mettler-Toledo C20S coulometer coupled to an analytical balance (0.01 mg resolution) and with Hydranal coulomat E as medium. Roughly 0.3 mL of solution were injected three times through the septum using a needled syringe and the mean value was calculated.The results are displayed in the table II.

Compounds	wet (as received)	dried
1-octadecene	42	0
hexane	28	0

TABLE II. Water contents (in ppm) of solvents used for the presented experiments obtained on triplicate measurements.

Powder X-Ray diffraction (XRD) data were acquired using a PANalytical Empyrean X-ray diffractometer using Cu Kα radiation (λ = 0.15418 nm) coupled with a PIXcel3D 2×2 area detector.

Elemental Analysis was carried out using a FLASH 2000 ThermoFisher CHNS/O analyzer with helium as carrying gas. Analyses have been performed in duplicate to ensure the accuracy of the result. The results are displayed in the

table III.

Sample name	N	C	H	O	Cd	total
$Cd(myr)_2$ A	0.00	59.15	9.83	11.94	17.81	98.73
$Cd(myr)_2$ B	0.00	59.88	9.78	12.29	18.48	100.43
Theory	0	59.32	9.6	11.28	19.82	100
$Cd(oleate)_2$ A	0.02	58.74	9.17	12.78	20.00	100.69
$Cd(oleate)_2$ B	0.00	62.99	9.89	11.07	16.05	100.00
Theory	0	64.06	9.79	9.49	16.67	100

TABLE III. Mass fractions obtained from elemental analysis on the four cadmium precursors.

V. SYNTHESIS PROTOCOLS

Cadmium(II) carboxylates preparation

$Cd(oleate)_2$ A. In a 1L three neck round bottom flask, 12.1776 g (40 mmol) of sodium oleate are dissolved in 200 mL ethanol at 70 °C. In parallel, 6.1996 g (20 mmol) of cadmium nitrate tetrahydrate are dissolved in 50 mL ethanol in a erlenmeyer flask. The cadmium nitrate tetrahydrate solution is then added dropwise over 30 min. The mixture is left during 2 hours. The reaction is then vacuum filtered (porosity 4) and the solid is washed 4 times with hot ethanol and two additional times with methanol. Then, solid is left to dry under vacuum overnight before use.

$Cd(myr)_2$ A. In a 1L three neck round bottom flask, 9.3 g (37 mmol) of sodium myristate are dissolved in 750 mL ethanol at room temperature. Meanwhile, 3.7 g (12 mmol) of cadmium nitrate tetrahydrate are dissolved in 120 mL ethanol in an erlenmeyer. The cadmium nitrate tetrahydrate solution is then added dropwise over 30 min. The mixture is left during 1 hours. The reaction is then vacuum filtered (porosity 4) and the solid is washed 3 times with methanol. Then, solid is left to dry under vacuum overnight before use.

$Cd(oleate)_2$ B. Cadmium(II) oleate was synthesized according to a procedure developed for lead(II) oleate [28]. Cadmium(II) oxide (3.85 g, 30 mmol) and acetonitrile (100 mL) are added to a 250 mL round bottom flask. The suspension is stirred while being cooled in an ice bath, after which trifluoroacetic acid (0.64 mL, 8.4 mmol, 0.3 equiv.) and trifluoroacetic anhydride (4.6 mL, 35 mmol, 1.1 equiv.) are added. After an hour the brown cadmium(II) oxide has dissolved, resulting in a clear and colorless solution that is allowed to warm to room temperature. Meanwhile, oleic acid (17.1 g, 61 mmol, 2 equiv) and triethylamine (10.7 mL, 77 mmol, 2.56 equiv) are mixed in a 2000 mL Erlenmeyer flask containing 370 mL of dichloromethane and 300 mL of acetonitrile at room temperature. The cadmium(II) trifluoroacetate solution is then added to the oleic acid solution with stirring, forming a white precipitate. The mixture is then placed in a -20 °C freezer and left overnight. The resulting white powder is isolated by vacuum filtration using a glass fritted funnel, the filtrate thoroughly washed with acetonitrile (5 × 100 mL) being careful to thoroughly stir the slurry to break up any large pieces, and then dried under vacuum overnight. The free-flowing white powder is stored in a nitrogen-filled glovebox. 19 g of white powder has been recovered, corresponding to a yield of 97 %. The purity can be confirmed by ^{1}H and ^{19}F NMR.

$Cd(myr)_2$ B. Cadmium(II) myristate was synthesized according to a procedure developed for lead(II) oleate [28]. Cadmium(II) oxide (9.5 g, 74 mmol) and acetonitrile (100 mL) are added to a 250 mL round bottom flask. The suspension is stirred while being cooled in an ice bath, after which trifluoroacetic acid (1.6 mL, 20.9 mmol, 0.3 equiv.) and trifluoroacetic anhydride (11 mL, 83 mmol, 1.1 equiv.) are added. After an hour, the brown cadmium(II) oxide dissolves, resulting in a clear and colorless solution that is allowed to warm to room temperature. Meanwhile, myristic acid (33.8 g, 148 mmol, 2 equiv) and triethylamine (26.3 mL, 195 mmol, 2.6 equiv) are mixed in a 2000 mL Erlenmeyer flask containing 740 mL of dichloromethane and 600 mL of acetonitrile at room temperature. The cadmium(II) trifluoroacetate solution is then added to the myristic acid solution while vigorously stirred, forming a white precipitate. The mixture is then placed in a -20 °C freezer and left overnight. The resulting white powder is isolated by vacuum filtration using a glass fritted funnel, the filtrate thoroughly washed with acetonitrile (3 × 250 mL) and diethyl ether (2 × 200 mL) being careful to thoroughly stir the slurry to break up any large pieces, and then dried under vacuum overnight. The free-flowing white powder is stored in a nitrogen-filled glovebox. 40 g of white powder has been recovered, corresponding to a yield of 95 %. The purity can be confirmed by ^{1}H and ^{19}F NMR.

CdSe nanoplatelets synthesis

5 ML CdSe NPL (first set of experimental conditions = protocol 1). 808 mg (1.2 mmol) of cadmium oleate, 54 mg (0.6 mmol) of selenium powder and 25 mL ODE are inserted in a 50 mL three-neck round bottom flask. This mixture is degassed under a vacuum for one h. The temperature is then raised to 240 °C under argon flow. At 205 °C, when the color is yellow-orange, 208 mg (0.8 mmol) of cadmium acetate dihydrate are swiftly injected. The mixture's color shifted from yellow-orange to deep red. Annealing at 240 °C is carried out for 10 min before injecting 1 mL of oleic acid and cooling down the flask to room temperature using a water bath. NPLs are separated from the unreacted species and quantum dots by centrifuging the crude mixed with 30 mL hexane and 30 mL isopropanol (in three separate 50 mL falcon tubes) during 30 min at 4838 g. Further purification by centrifugation at 4838 g (10 min) were carried out in presence of 4 mL isopropanol to remove the remaining quantum dots. After each centrifugation, NPLs are re-dispersed in 5 mL hexane.

4 ML CdSe NPL (first set of experimental conditions = protocol 1). 340 mg (0.6 mmol) of cadmium myristate, 24 mg (0.3 mmol) of selenium powder and 30 mL ODE are inserted in a 50 mL three-neck round bottom flask. This mixture is degassed at 90 °C under vacuum for 1 h. The temperature is then raised to 240 °C under argon flow. At 205 °C, when the color is yellow, 110 mg (0.4 mmol) of cadmium acetate dihydrate are swiftly injected. The mixture's color shifted from yellow-orange to deep red to black. Annealing at 240 °C is carried out during 10 min before injecting 1 mL of oleic acid and cooling down the flask to room temperature using a water bath. Size-dependent purification was the same as for the 5 ML NPLs.

4 / 5 ML CdSe NPL (second set of experimental conditions = protocol 2). This second set of experimental conditions is similar to the one presented previously. However, extreme care was taken in **protocol 2** to remove water from the reactive medium. Indeed, solvents were dried and distilled prior to use. Moreover, flask loadings were performed inside a Ar-filled glovebox. Briefly, 340 mg (0.6 mmol)/ 808 mg (1.2 mmol) of $Cd(myr)_2$ / $Cd(oleate)_2$ B, 24 mg (0.3 mmol)/54 mg (0.6 mmol) of selenium powder and 25 mL ODE are loaded in a 50 mL three-neck round bottom flask in a glove box. 96 mg (0.4 mmol)/ 182 mg (0.8 mmol) cadmium acetate is loaded in a powder addition funnel and the whole setup is sealed, removed from the glovebox and cycled onto a Schlenk line. The mixture is degassed under vacuum for 1 h. The temperature is then raised to 240 °C under argon flow. At 205 °C, when the color is yellow-orange/ yellow, cadmium acetate is swiftly injected. The mixture's color shifted from yellow-orange to deep red (to black for 4 ML). Annealing at 240 °C is carried out during 10 min before injecting 1 mL of oleic acid and cooling down the flask to room temperature using a water bath.
Purification is carried in the same way as for the previously described 5 ML synthesis.

VI. HYDRATION OF $Cd(CO_2R)_2$

Hydrated $Cd(O_2CR)_2$ B precursors were obtained by exposing the starting precursor to a humid atmosphere. They were placed in a chamber with a controlled atmosphere set at 90 % relative humidity for three days. The precursors are then used without further purification.
As shown on the SAXS diagram on figure S1, the presence of hydroxide anions bonded to cadmium cation can be evidenced by harmonics with a corresponding distance of 2.26 nm and a shift from 3.70 nm to 3.58 nm for d_{m1}. The first distance falls within our expectation for two cadmium atoms separated by one myristate plus one hydroxide species (1.92 nm (one myristate unit) + 0.275 nm (metal-O_2C distance) + 0.110 nm (size of hydroxide moiety) = 2.31 nm)[46]. Such bonding would lower the hydrocarbon packing density, the ligand steric repulsion and d_{m1} by increasing interpenetration from 0.69 nm to 0.84 nm.

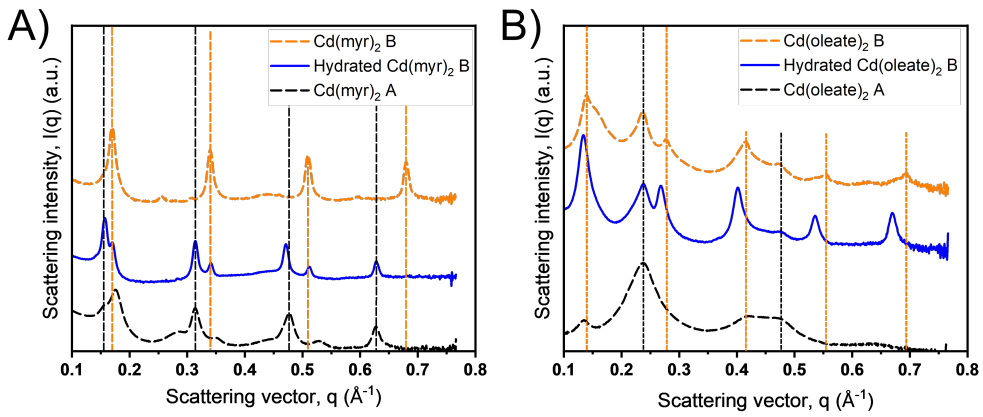

FIG. S1. SAXS diagrams of several A) $Cd(myr)_2$ and B) $Cd(oleate)_2$ precursors. *Note:* orange, black and blue curves correspond to precursors B, A and hydrated B, respectively.

TGA comparison of $Cd(oleate)_2$ B and hydrated $Cd(oleate)_2$ B has been performed. As shown on figure S2, similar loss profile is observed; however, the overall loss is higher in the case of the hydrated compounds. The residue after the annealing at 1000 °C corresponds to pure CdO with a minor amount of unidentified impurities. Water may be the cause of the higher loss; its presence is also confirmed by FT-IR analysis. It is worth noting that the first weight loss occurs, in the case of the hydrated sample, at a lower temperature than expected: from 50 to 100 °C.

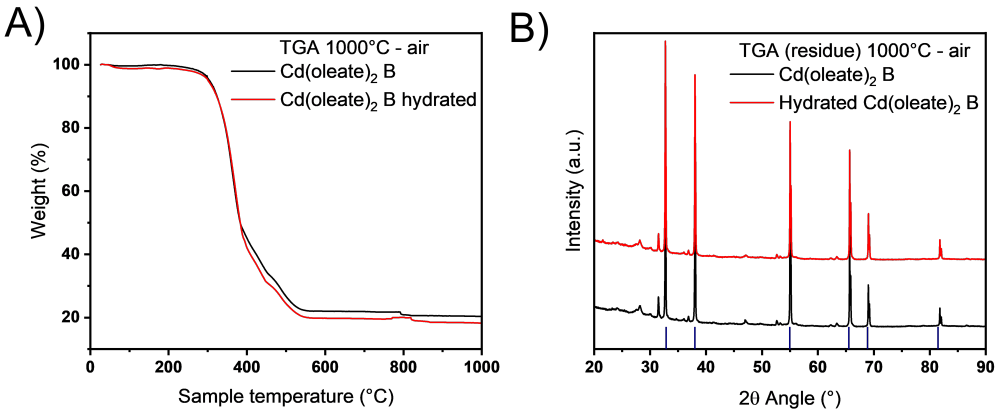

FIG. S2. Thermogravimetric analysis and X-ray diffractogram of A) $Cd(oleate)_2$ B and hydrated $Cd(oleate)_2$ B. *Note:* TG analyses were performed at a heating rate of 5 $K.min^{-1}$ and XRD were acquired using Kα Cu radiation. Blue marks correspond to CdO diffraction peaks calculated from ICDD file n° 73-2245.

As stated in the main text, QD formation and growth mechanism solely depend on the structure of the cadmium precursor. Figure S3 presents the *in situ* SAXS results employing hydrated forms of $Cd(O_2CR)_2$ B. The observed

trend is the same as for $Cd(oleate)_2$ and $Cd(myr)_2$, leading to the formation of 4 ML NPLs. That is the complete disappearance of the lamellar Bragg peaks before selenium dissolution. One notable difference is the first nanocrystal apparition at 180 and 190°C due to higher water content. We believe the synthesized NPL thickness depends on the structure and the solubilization of the cadmium precursors rather than the water impurities it contains.

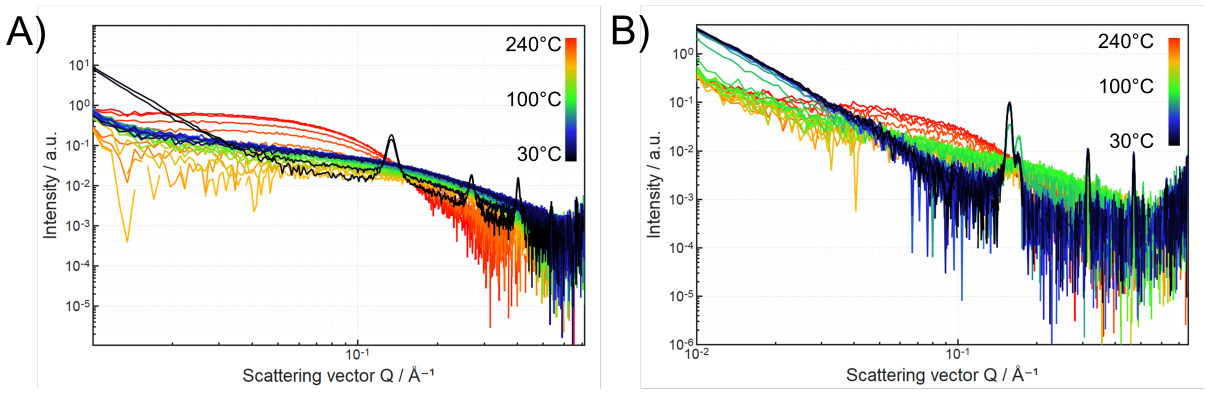

FIG. S3. SAXS pattern of the cadmium precursors dissolution and the growth of CdSe quantum dots corresponding to A) hydrated $Cd(oleate)_2$ B and B) hydrated $Cd(myr)_2$ B.

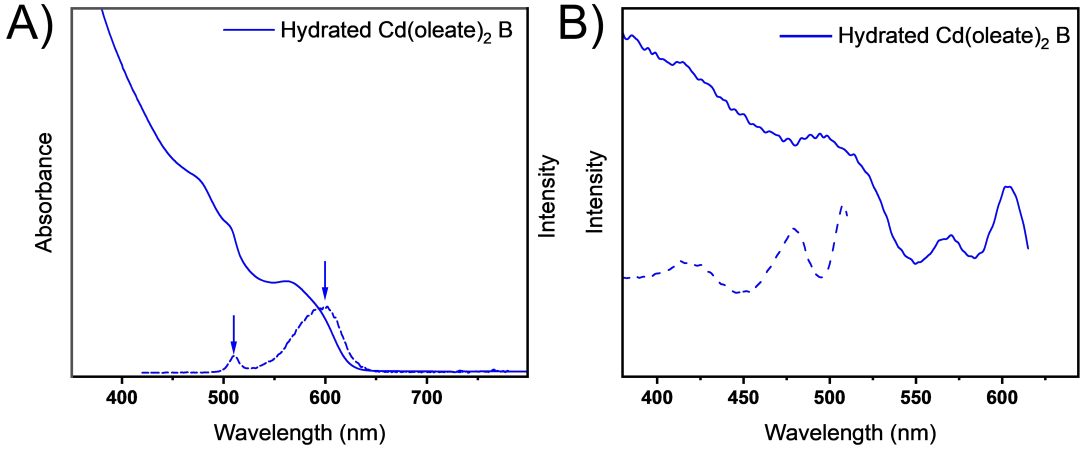

FIG. S4. UV-Vis absorbance (plain) and PL (dashed) spectra of QDs obtained after *in situ* Linkam experiments involving $Cd(oleate)_2$ A) and PLE spectra B) corresponding to the arrows in A. *Note*: in B) plain and dash traces correspond to emissions centered at 600 nm and 507 nm, respectively.

VII. SUPPLEMENTARY FIGURES

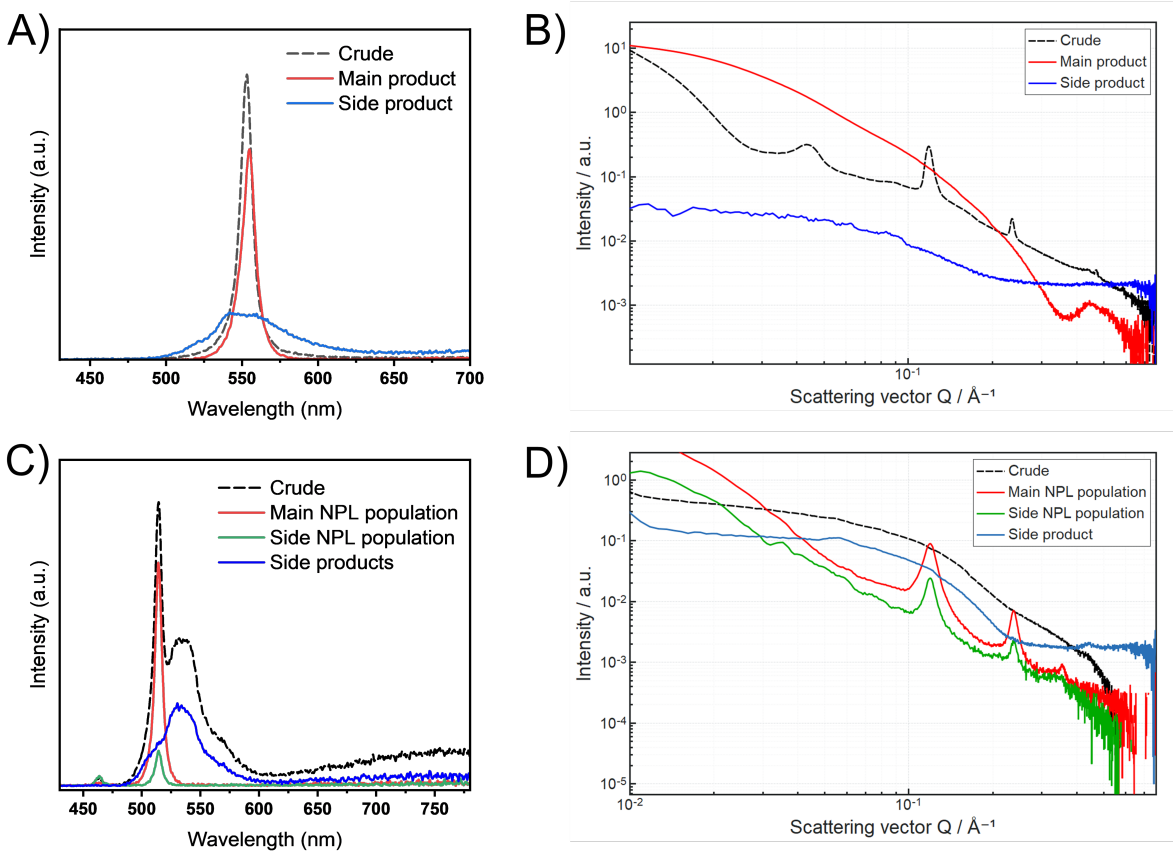

FIG. S5. Emission spectra and SAXS pattern of syntheses involving $Cd(oleate)_2$ A in **protocol 1** (A and B) and $Cd(oleate)_2$ B following **protocol 2** (C and D). *Note:* SAXS pattern displays typical signatures for nanoplatelets (B red trace) and of nanospheres (B,D blue traces). A Bragg peak related to the NPL stacking is usually observed for the crude (black line in B) as ODE is a bad solvent for the NPLs. Similar stacking peaks are observed for the 4 and 3 ML NPL suspension in hexane (D red and green traces). No stacking peak is observed for the crude.

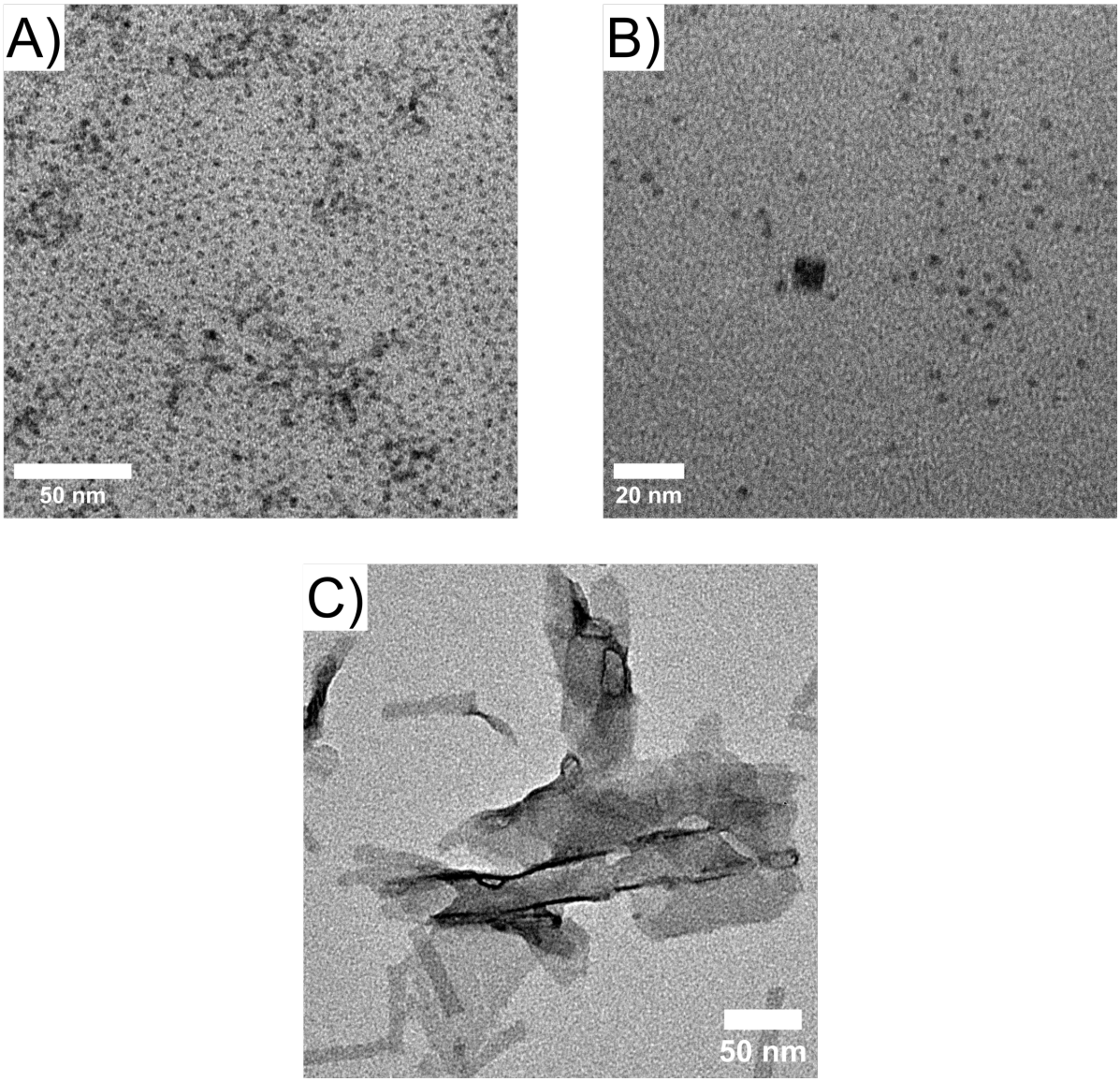

FIG. S6. TEM images of A) quantum dots obtained as side-products for the synthesis of 5 ML NPLs employing $Cd(oleate)_2$ A following **protocol 1**, B) quantum dots obtained *via* the use of $Cd(oleate)_2$ B in **protocol 2** and C) 3 ML NPLs obtained using $Cd(oleate)_2$ A following **protocol 1**. *Note:* the 3 ML adopt a helix configuration.

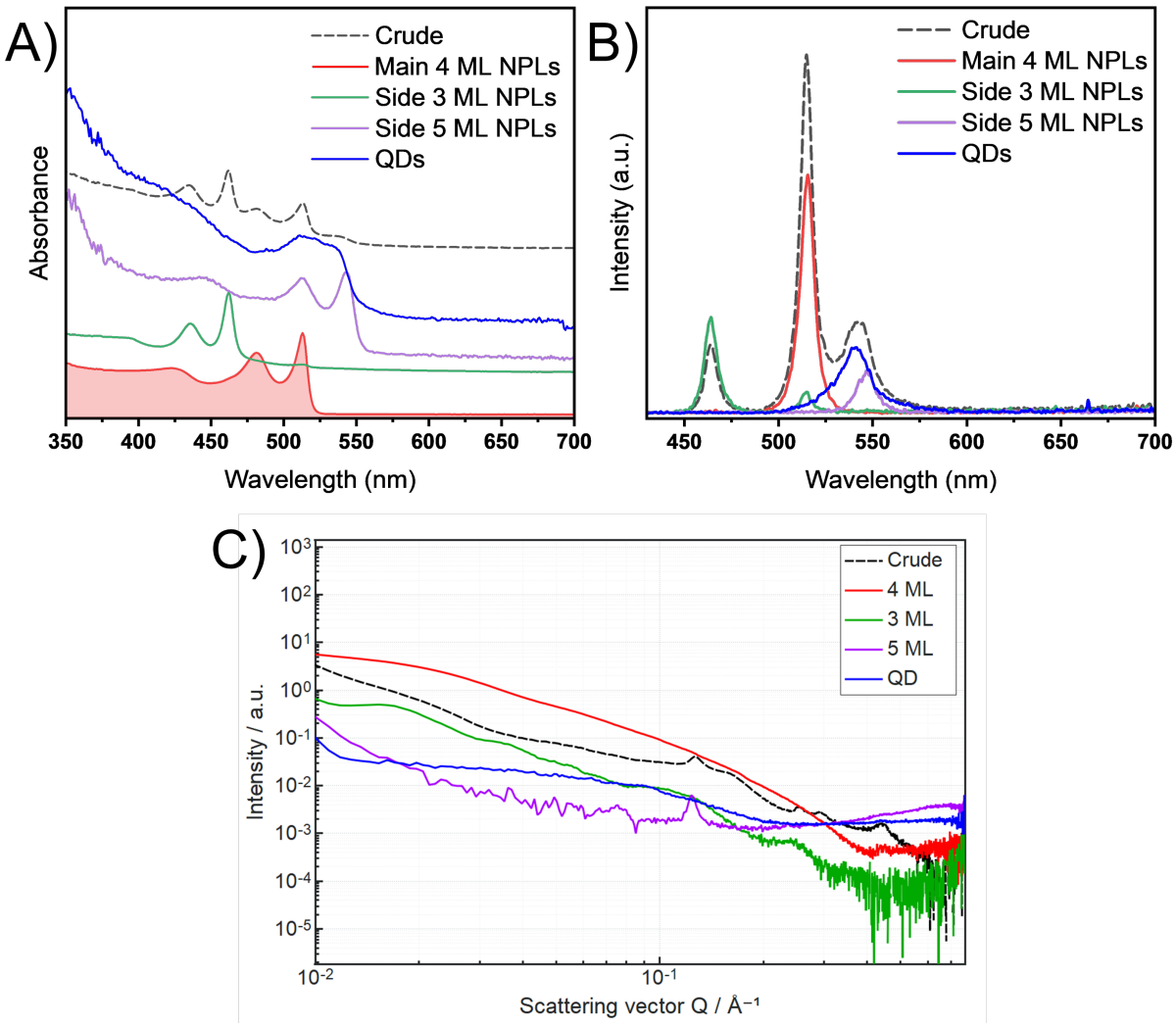

FIG. S7. Results of 4 ML NPL syntheses using $Cd(myr)_2$ A with **protocol 1**. A) UV-Vis spectra and B) emission spectra of the crude and the different isolated fractions. "Main" NPL population corresponds to the desired NPL, which are 4 ML in that case. C) is the SAXS pattern of the NPL isolated fractions in hexane. *Note:* SAXS patterns for 4 ML NPLs (red trace), 3 ML NPLs (green trace) display typical features: a q^{-2} slope and oscillations, highlighting the enrolled nature of the 3 ML NPLs, respectively.

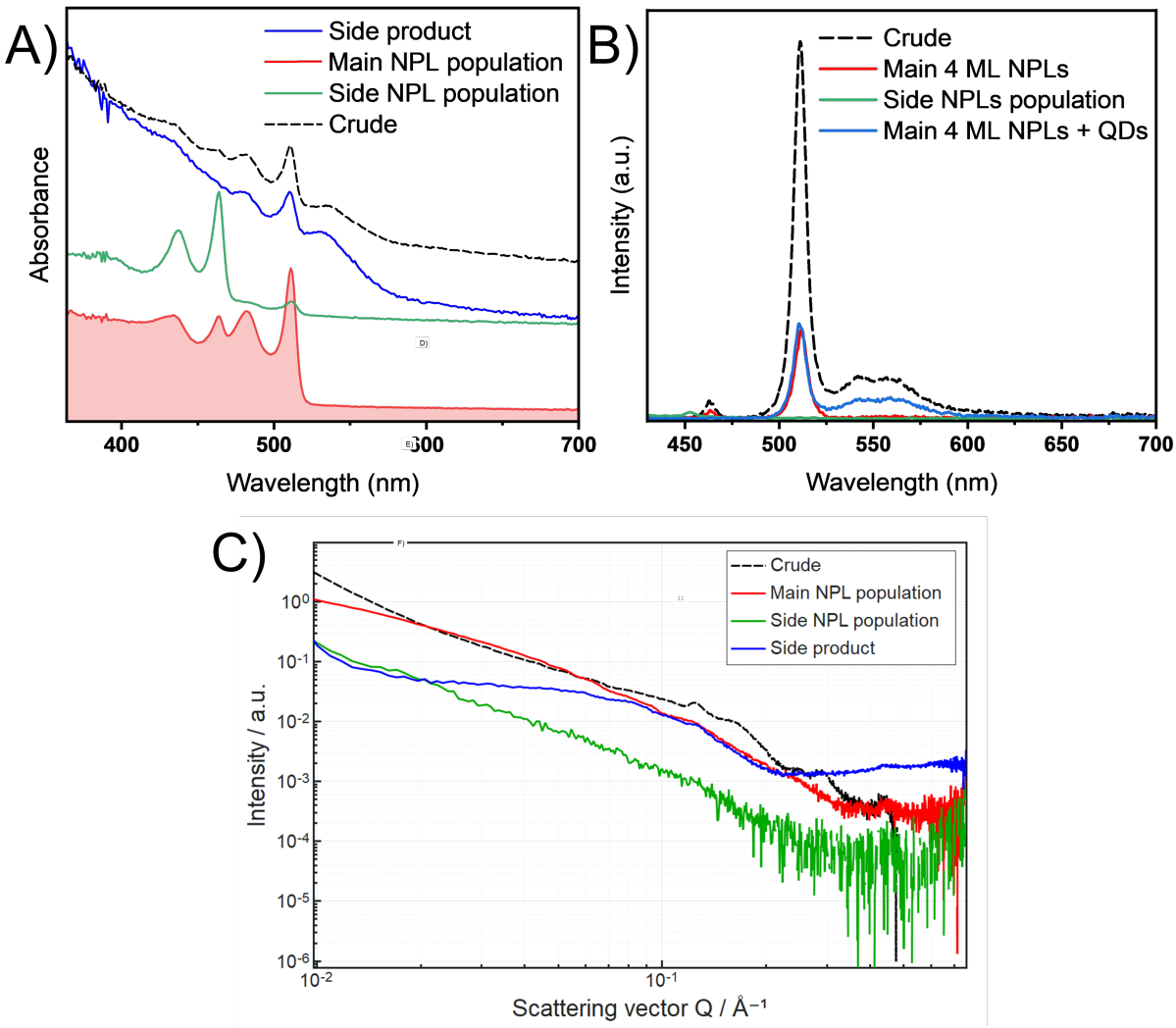

FIG. S8. Results of 4 ML NPL syntheses using $Cd(myr)_2$ B following **protocol 2**. A) UV-Vis spectra and B) emission spectra of the crude and the different isolated fractions. "Main" NPL population corresponds to the desired NPL which are 4 ML in that case. C) is the SAXS pattern of the NPL isolated fractions in hexane.

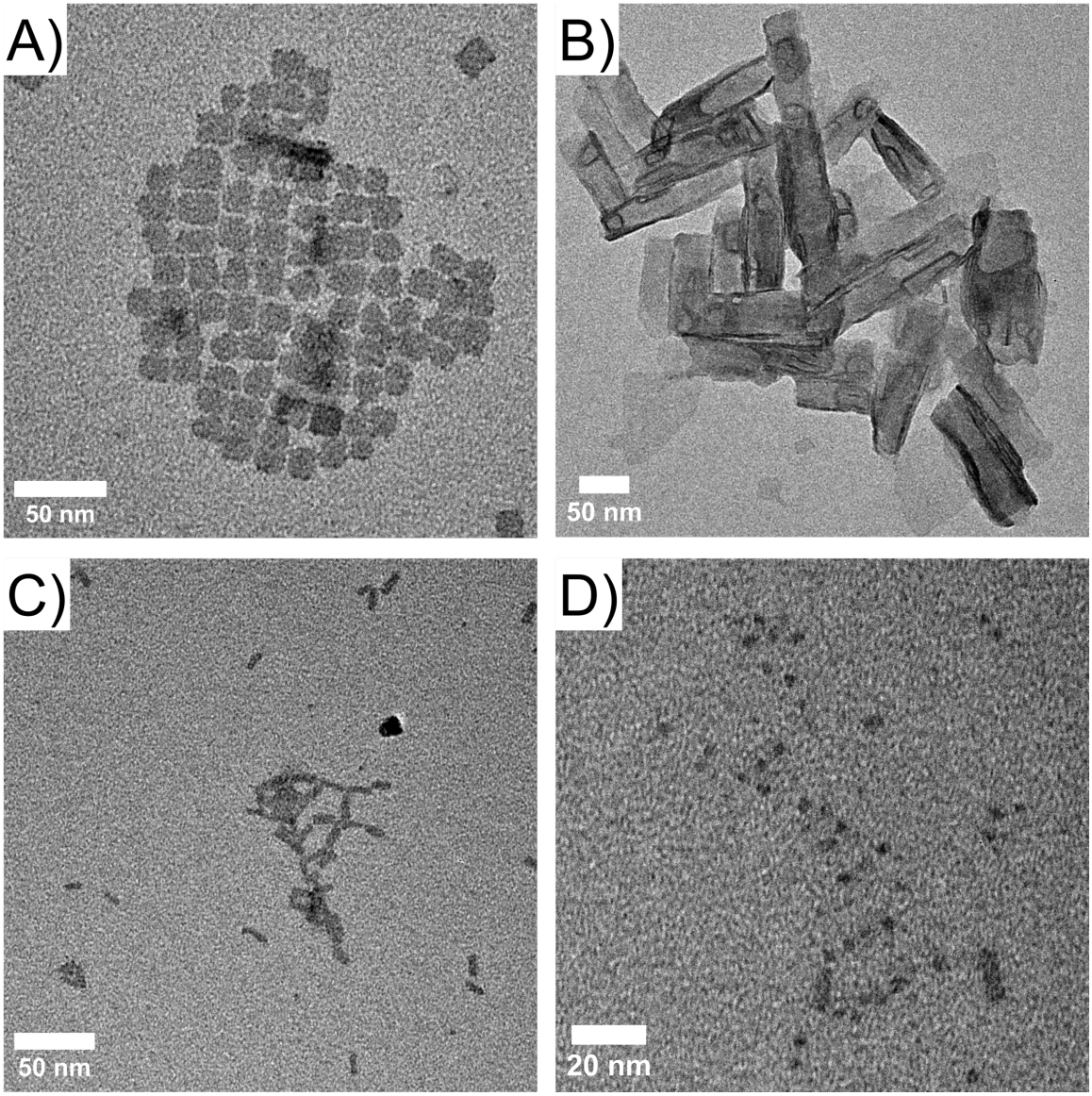

FIG. S9. TEM images of the isolated products issued from 4 ML NPL synthesis using $Cd(myr)_2$ A and following **protocol 1**. A) 4 ML NPLs, B) cylindrically enrolled 3 ML NPLs, C) 5 ML NPLs, and D) QDs. Correspond to A) 4 ML NPLs, B) 3 ML NPLs, C) 5 ML NPLs and D) quantum dots.

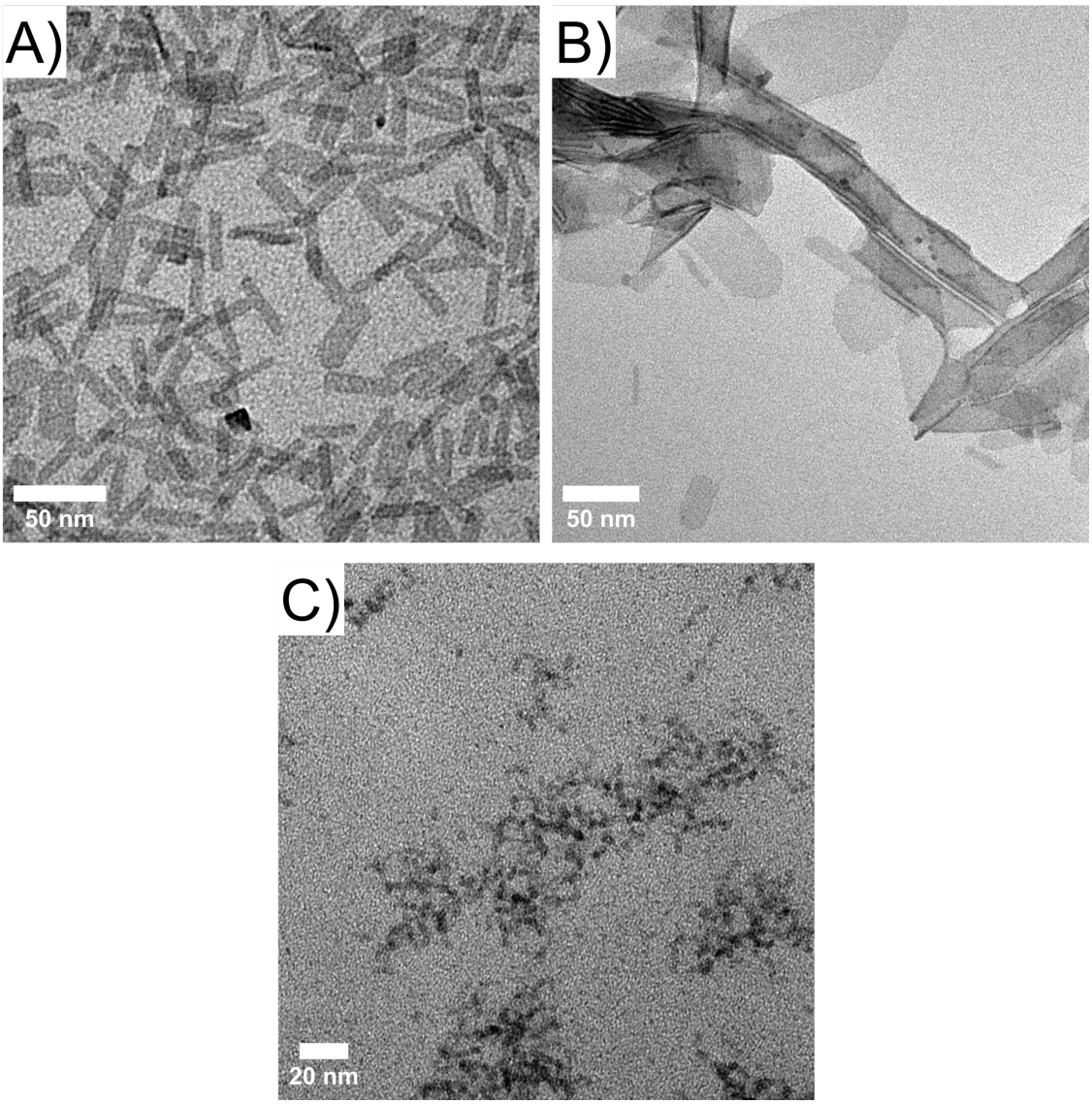

FIG. S10. TEM images of the isolated products issued from 4 ML NPL synthesis using $Cd(myr)_2$ B and **protocol 2**. A) corresponds to the main 4 ML NPL population, B) the side 3 ML NPL population and C) side products. Lateral size polydispersity hypothesized to rationalize the NPLs mixture observed in UV-Vis can be confirmed with these pictures. Interestingly, these rolled 3 ML NPLs adopt a helical ribbon conformation consistent with what was discussed for the previous SAXS pattern.

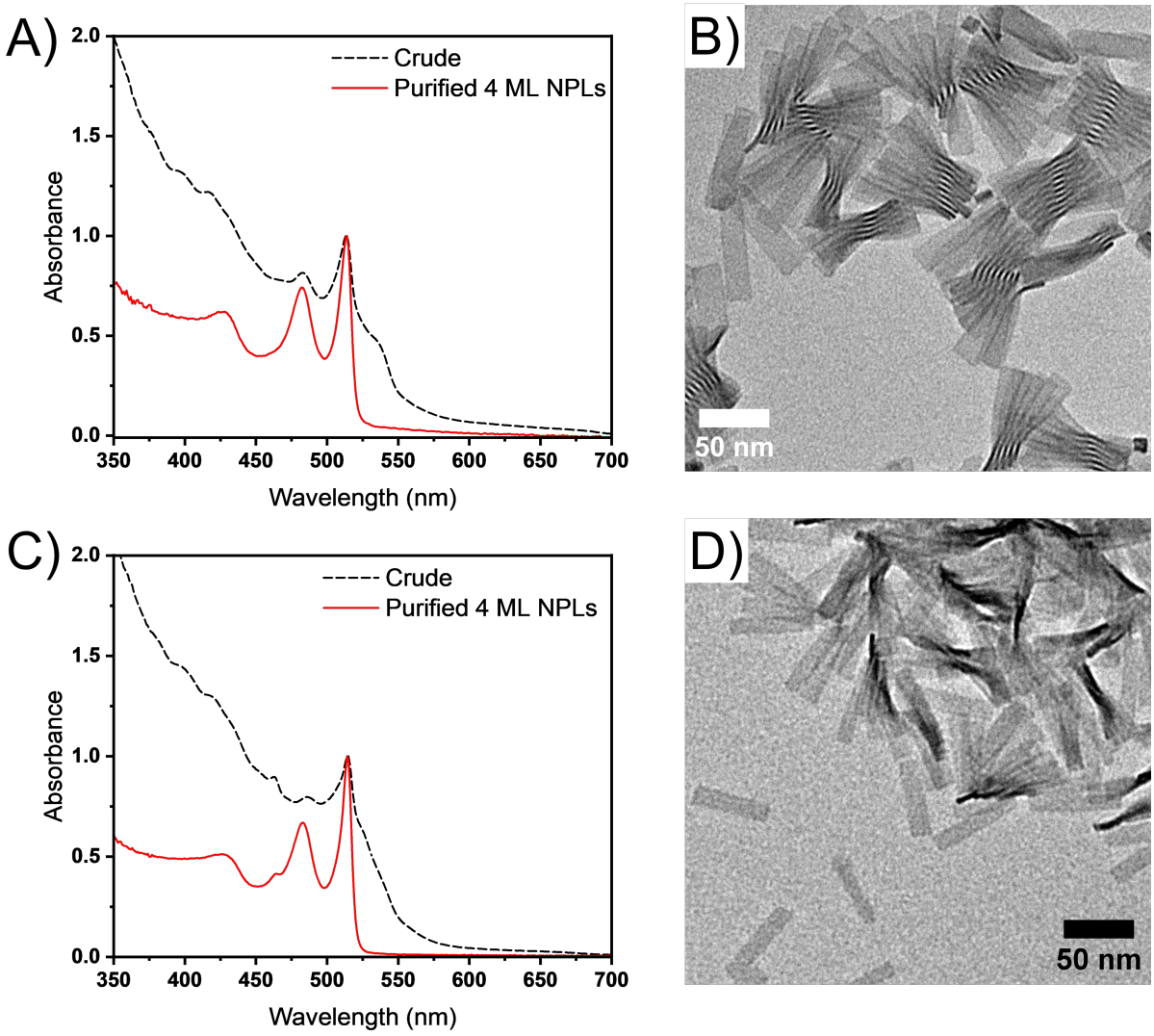

FIG. S11. UV-Vis spectra and TEM images for the crude and the main population of purified 4 ML NPL population using (A and B) $Cd(oleate)_2$ B/**protocol 1** and (C and D) $Cd(oleate)_2$ B/**protocol 2**. *Note:* 3 and 4 ML NPLs lateral size distributions seems to be sufficiently apart from each other to enable efficient size-selective separation as evidenced by UV-Vis.

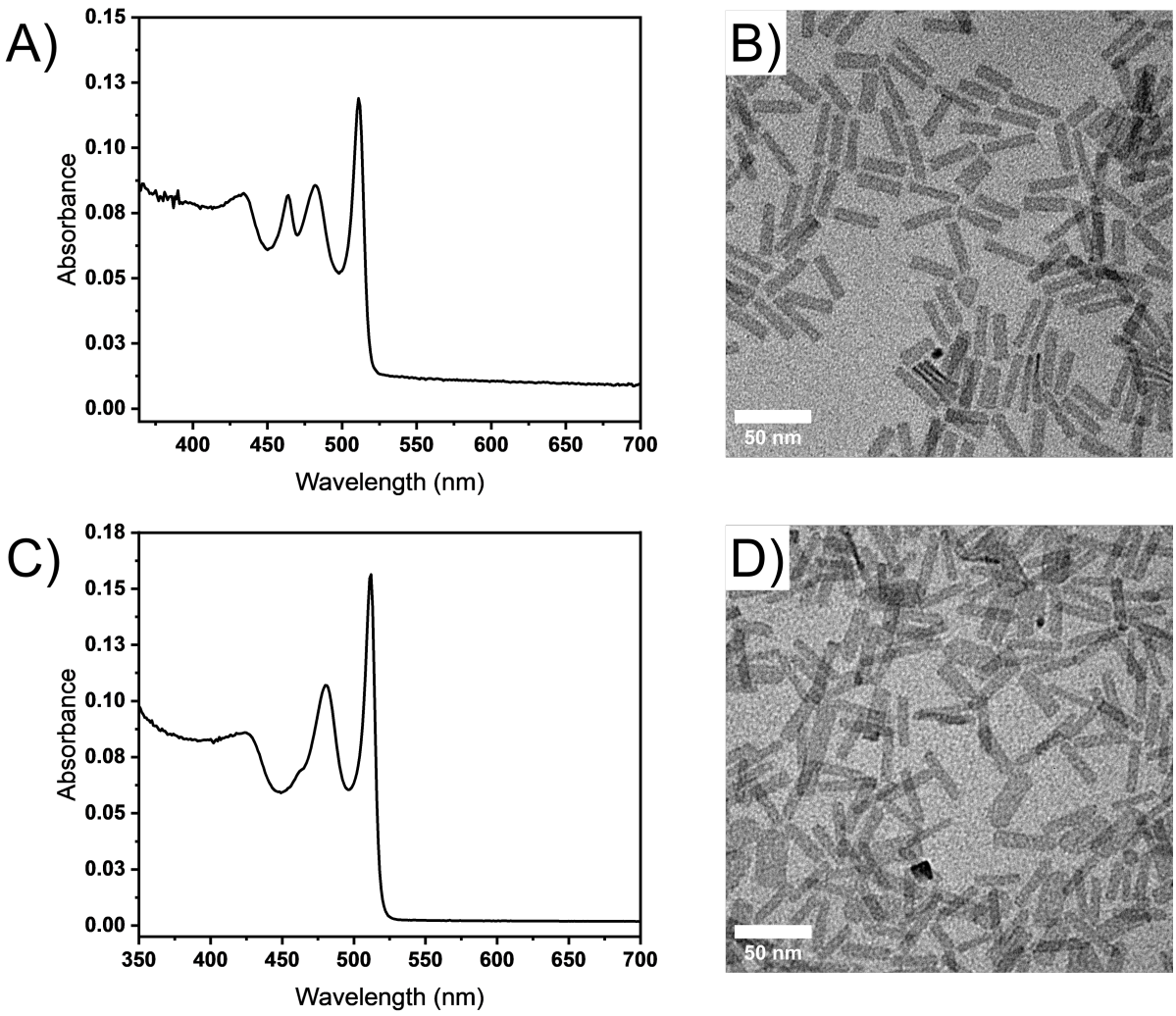

FIG. S12. UV-Vis spectra and TEM images for the crude and the main population of purified 4 ML NPL population using (A and B) $Cd(myr)_2$ B/**protocol 1** and (C and D) $Cd(myr)_2$ B/**protocol 2**. *Note:* 3 and 4 ML NPLs lateral size distributions seems to be sufficiently apart from each other to enable efficient size-selective separation as evidenced by UV-Vis.

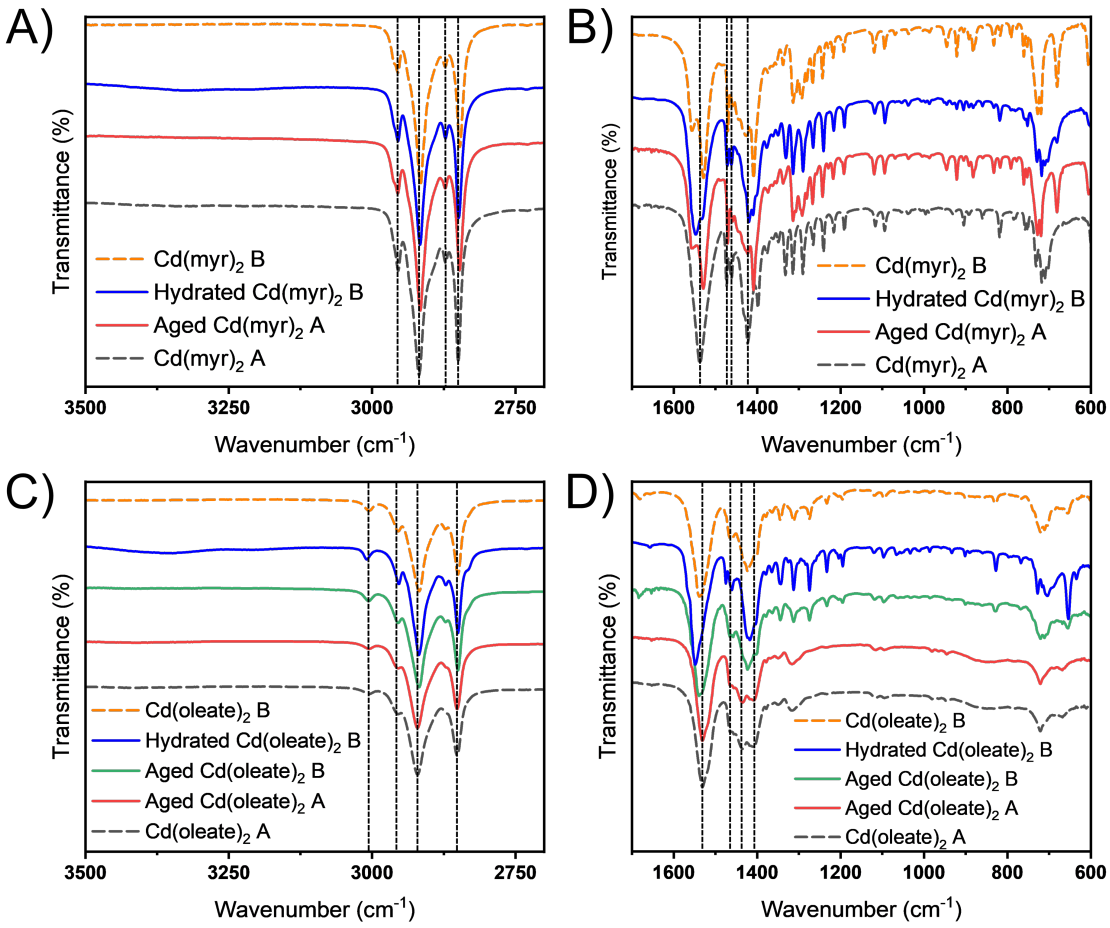

FIG. S13. FT-IR spectra of A) and B) $Cd(myr)_2$ precursors and of C) and D) $Cd(oleate)_2$ precursors. Vertical dotted lines are added to ease band comparisons with $Cd(oleate)_2$ A.

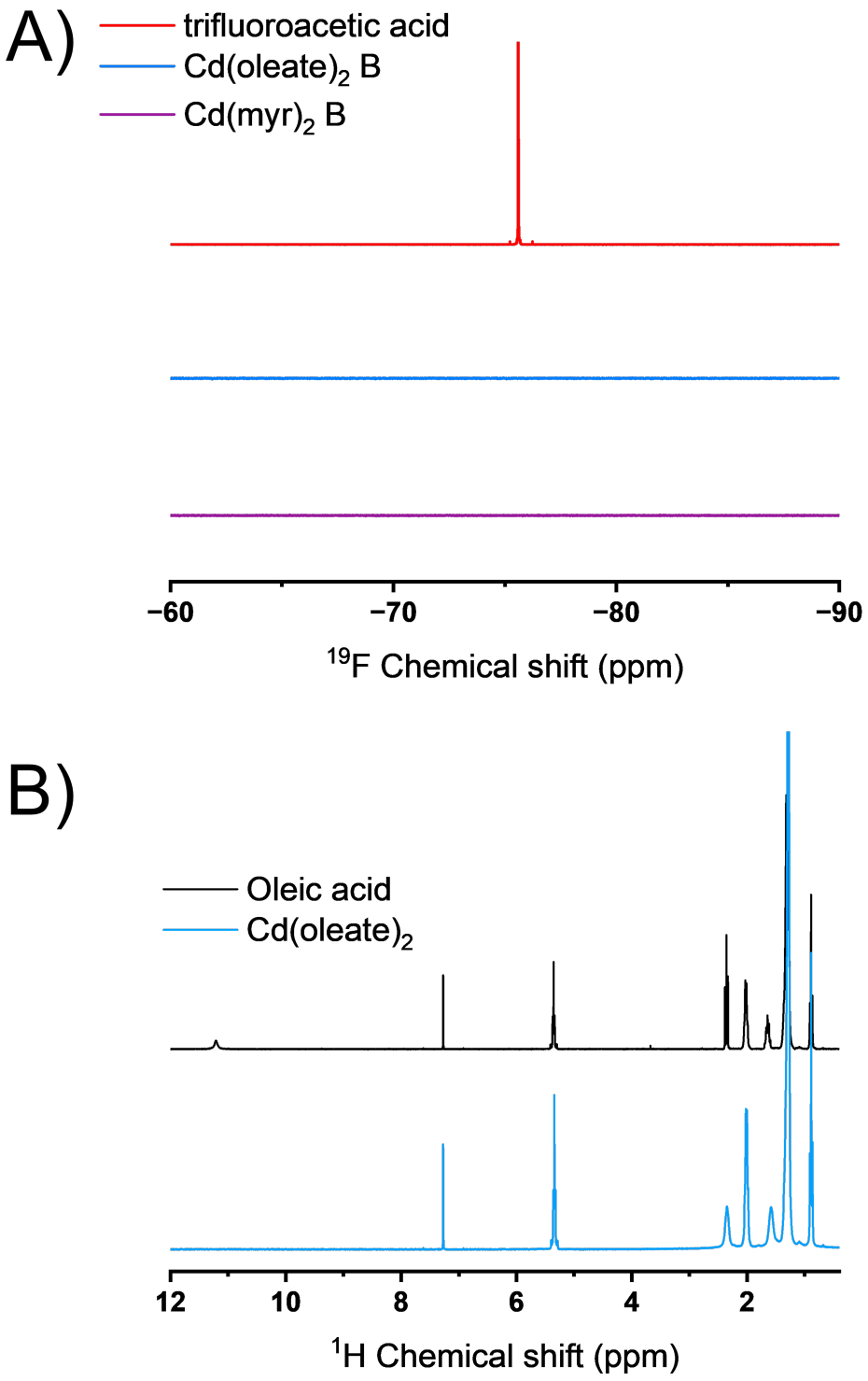

FIG. S14. A) ^{19}F NMR spectra of trifluoroacetic acid, $Cd(myr)_2$ and $Cd(oleate)_2$. B) ^{1}H NMR spectra of oleic acid and $Cd(oleate)_2$ ($[Cd(oleate)_2]$ = 20 mM). *Note:* All experiments performed in *d*-chloroform and $Cd(myr)_2$ was heated prior to measurements but started to precipitate during ^{1}H NMR acquisition so the spectrum is not displayed.

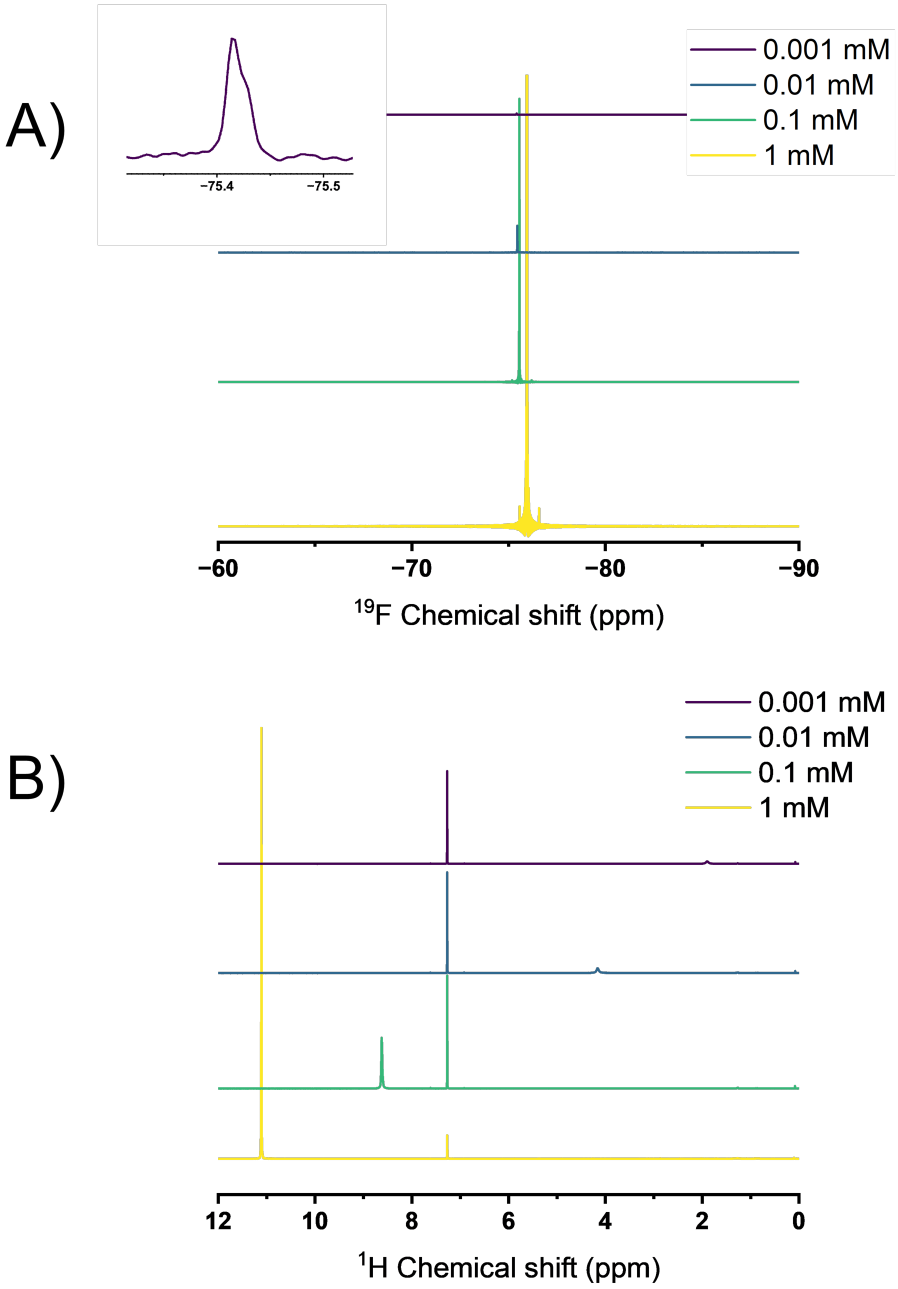

FIG. S15. A) ^{19}F and B) ^{1}H NMR spectra of trifluoroacetic acid (TFA) in *d*-chloroform with various concentrations allowing the assessment of the limit of detection of TFA. *Note*: all the analysis are performed in a quantitative way allowing for direct comparison of the signal intensities. Insert in figure A) represents a zoom in on the TFA signal for a concentration of 0.001 mM.

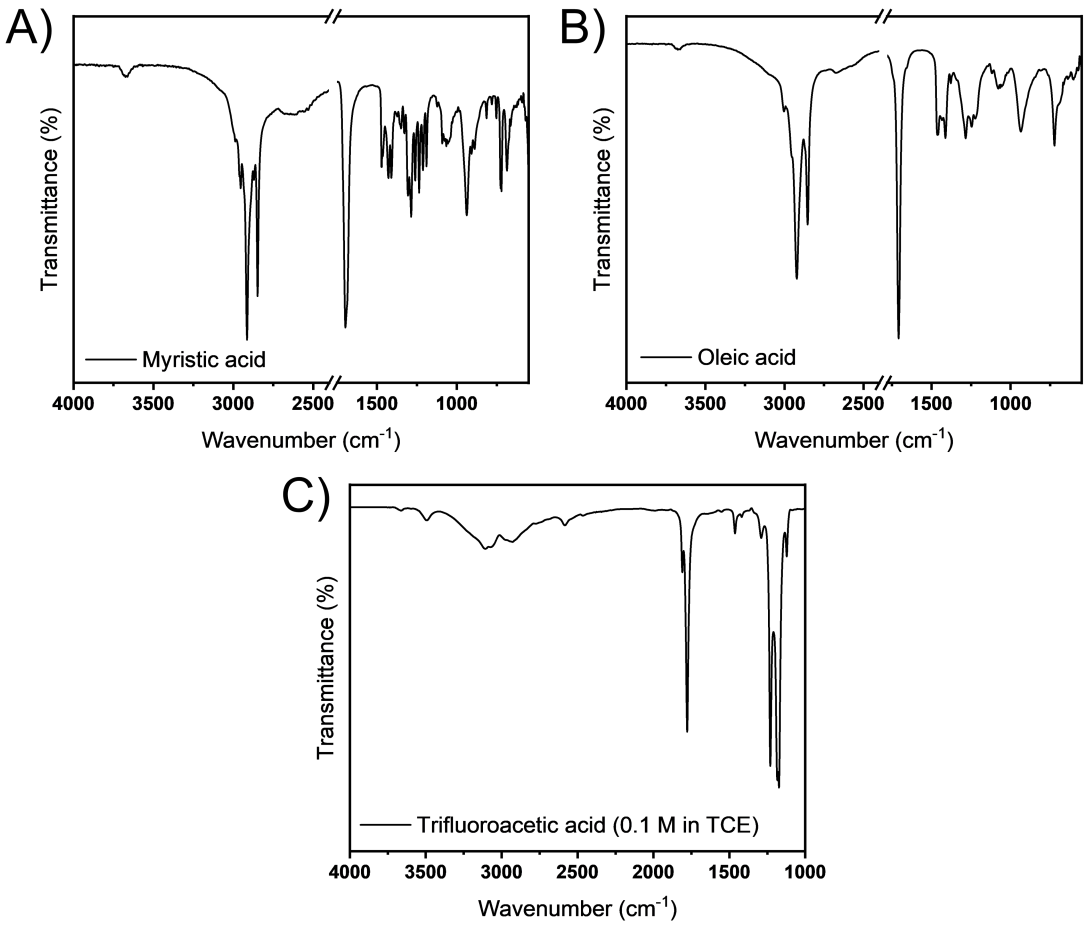

FIG. S16. FT-IR spectra of A) myristic acid, B) oleic acid, and C) trifluoroacetic acid. $Cd(myr)_2$ and $Cd(oleate)_2$ and B) ^{19}F NMR spectra of trifluoroacetic acid. *Note:* trifluoroacetic acid was recorded in transmission mode as a solution in tetrachloroethylene (TCE - 0.1 M).

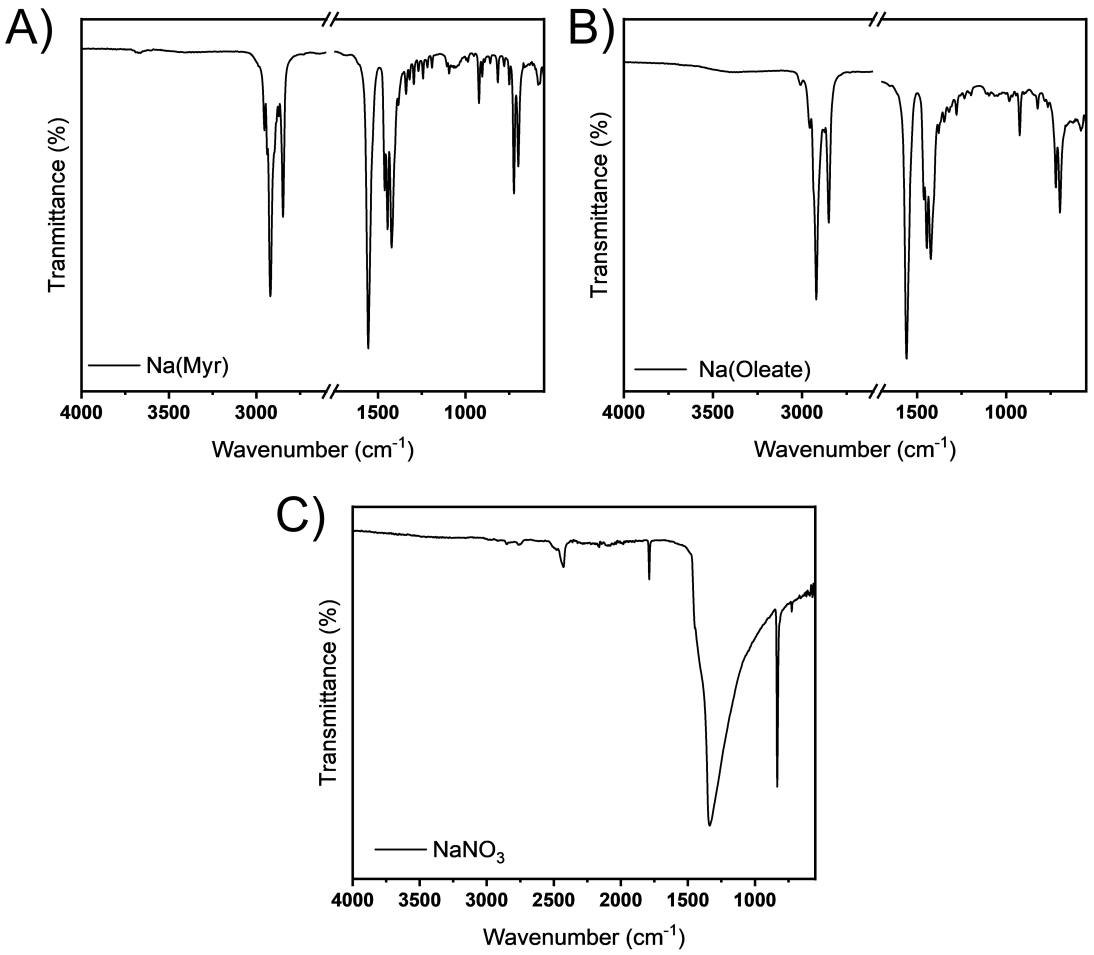

FIG. S17. FT-IR spectra of A) sodium myristate (Na(myr)), B) sodium oleate (Na(oleate)) and C) sodium nitrate ($NaNO_3$).

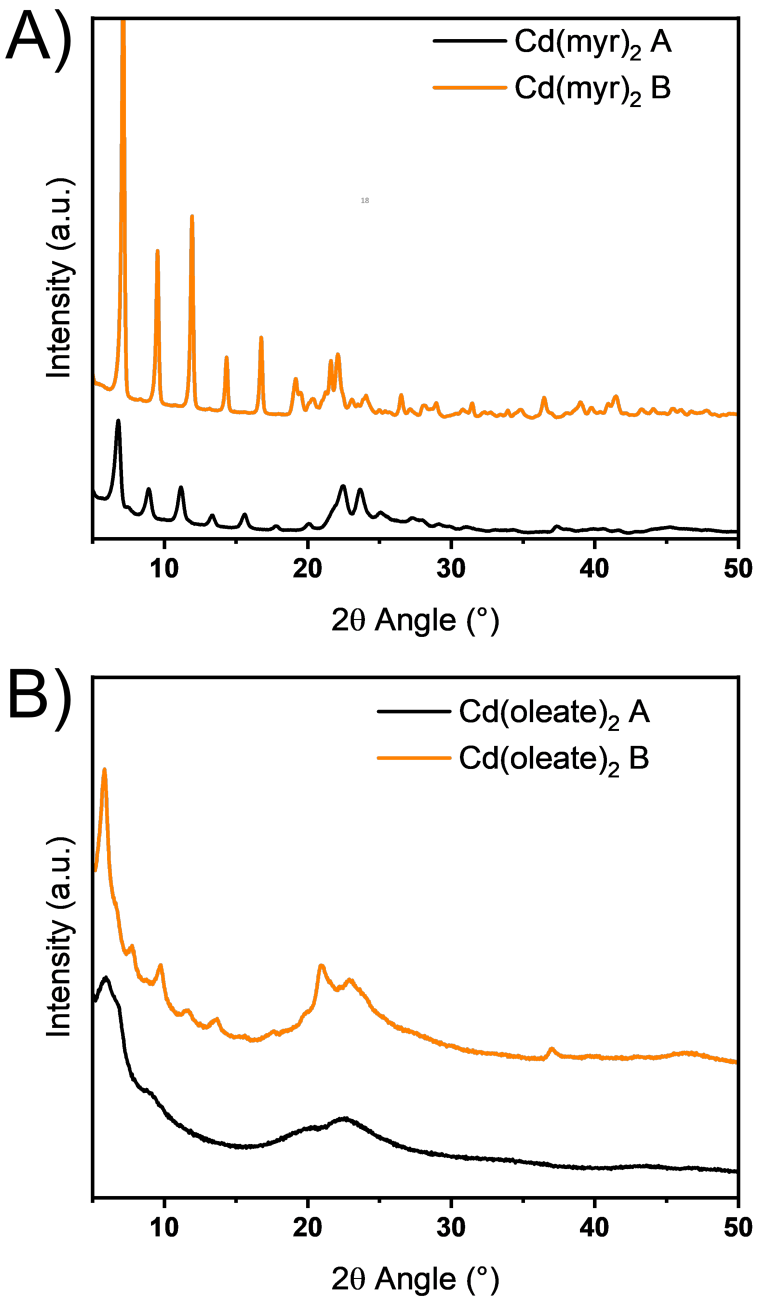

FIG. S18. XRD patterns of A) $Cd(myr)_2$ and B) $Cd(oleate)_2$.

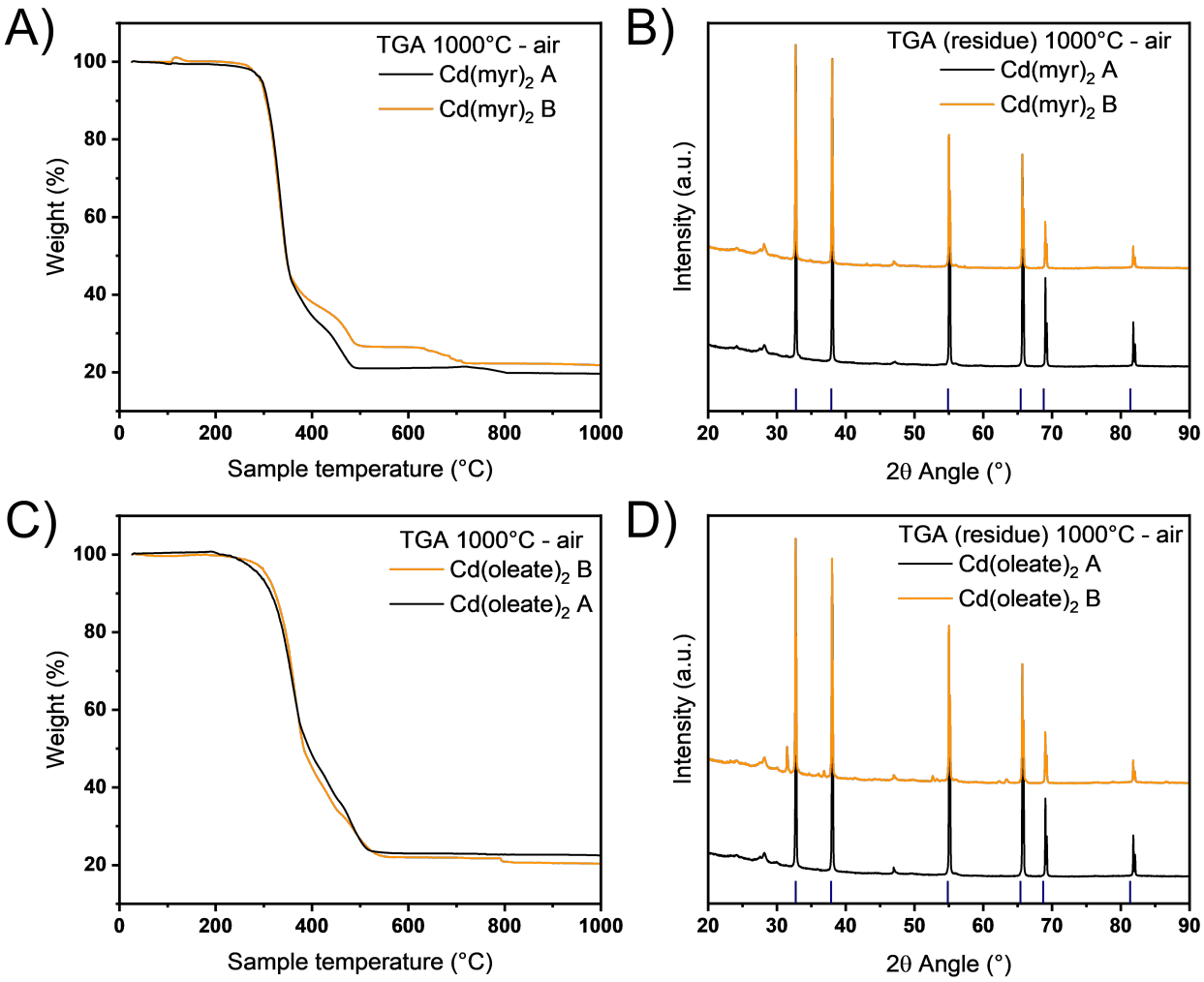

FIG. S19. Thermogravimetric analyses and X-ray diffractograms of $Cd(myr)_2$ (A-B) and $Cd(oleate)_2$ (C-D). *Note:* TG analyses were performed at a heating rate of 5 $K.min^{-1}$ and XRD were acquired using Kα Cu radiation. Blue marks correspond to CdO diffraction peaks calculated from ICDD file n° 73-2245.

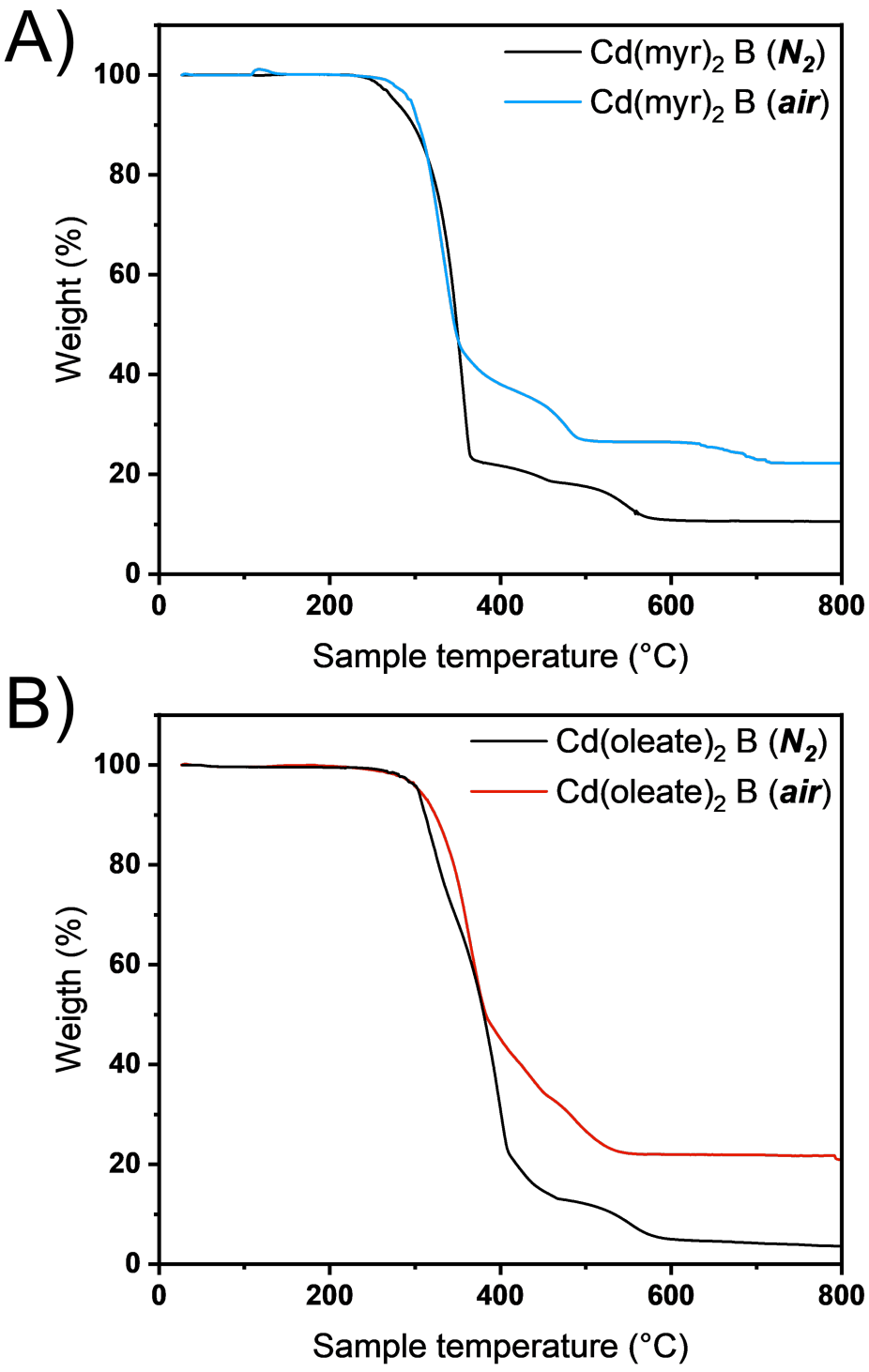

FIG. S20. Comparison between thermogravimetric analyses performed in air and nitrogen of A) $Cd(myr)_2$ and B) $Cd(oleate)_2$. *Note:* TG analyses were performed at a heating rate of 5 $K.min^{-1}$.

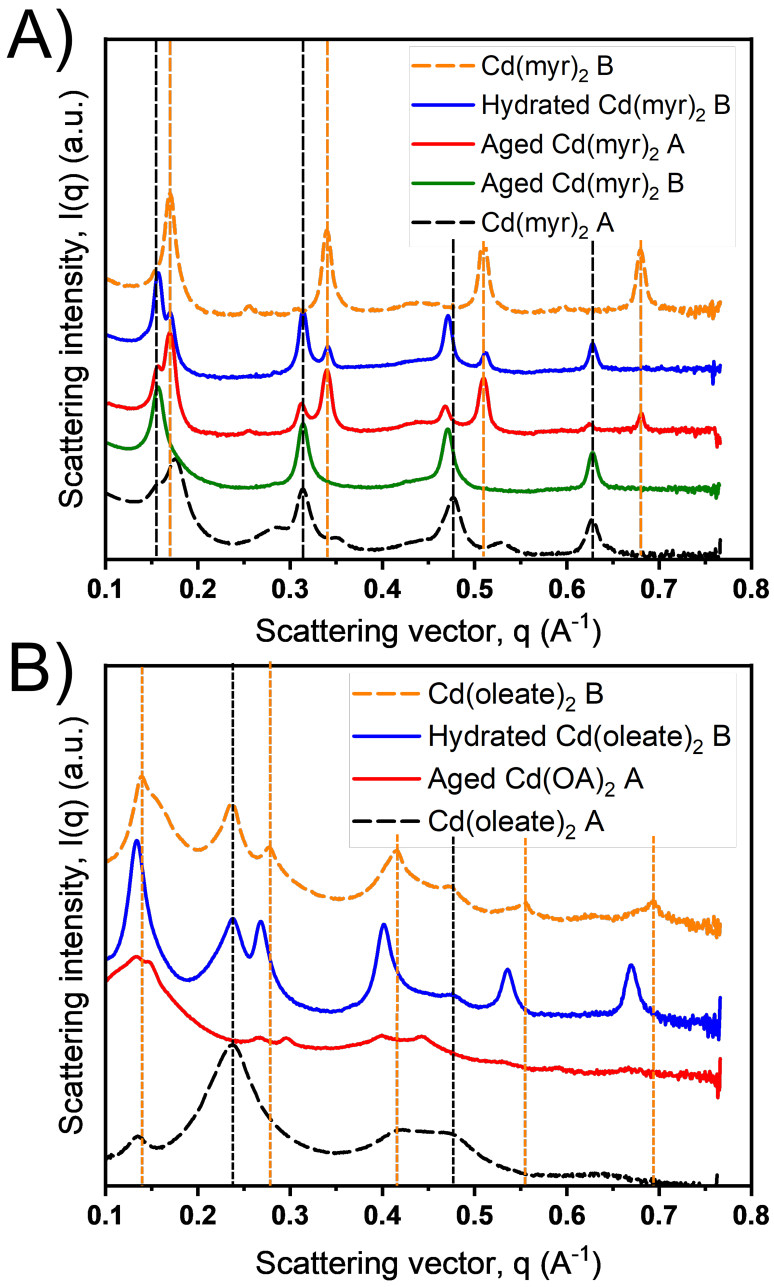

FIG. S21. SAXS patterns for A) $Cd(myr)_2$ and B) $Cd(oleate)_2$ precursors that have either been hydrated or aged (see methods for further details). The unmodified cadmium carboxylate (A or B) is added for comparison in a dotted line. Vertical dotted lines are added to help the peak position comparisons.

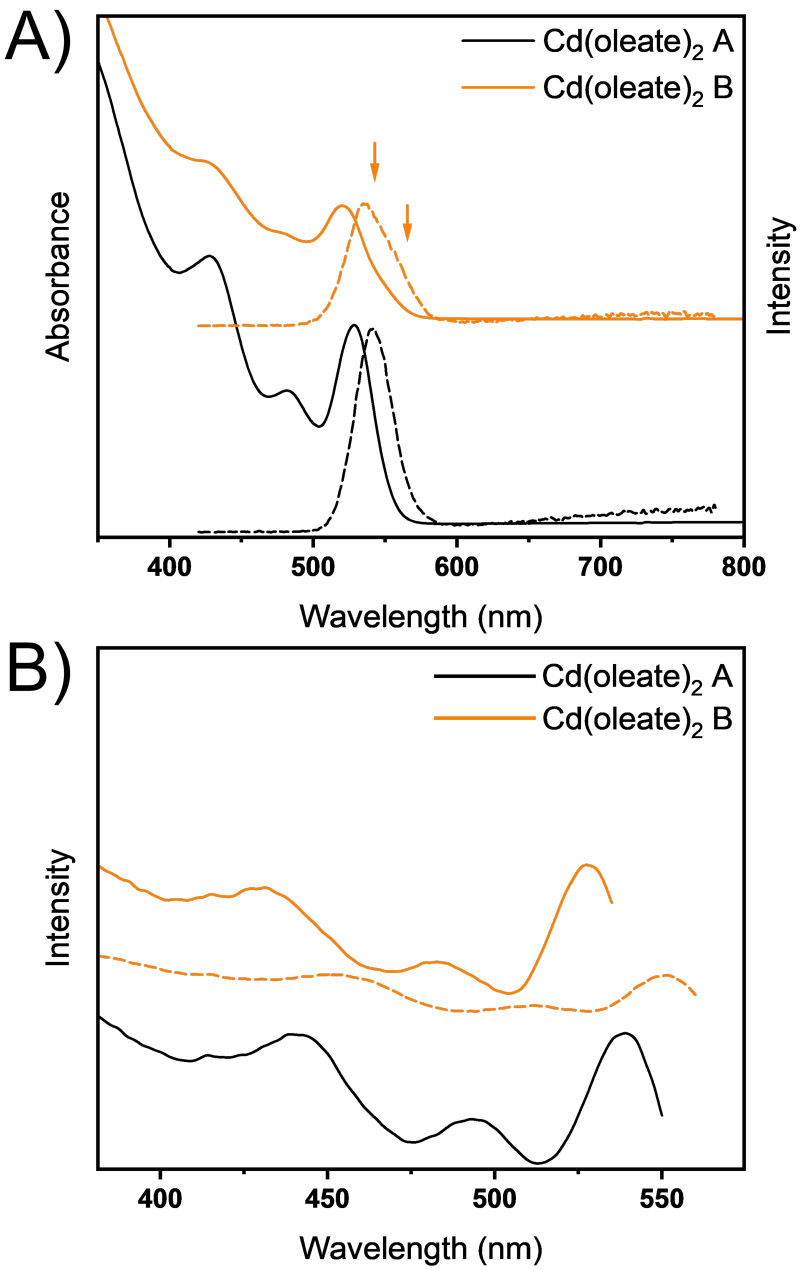

FIG. S22. A) UV-Vis and emission spectra and B) excitation spectra of the obtained quantum dots suspended in hexane after the Linkam temperature rise starting from several $Cd(oleate)_2$ precursor. The orange arrows in A) represent wavelengths used for the excitation spectra displayed in B). Solid lines in B) are for the main product, whereas dotted ones are for the minor product.

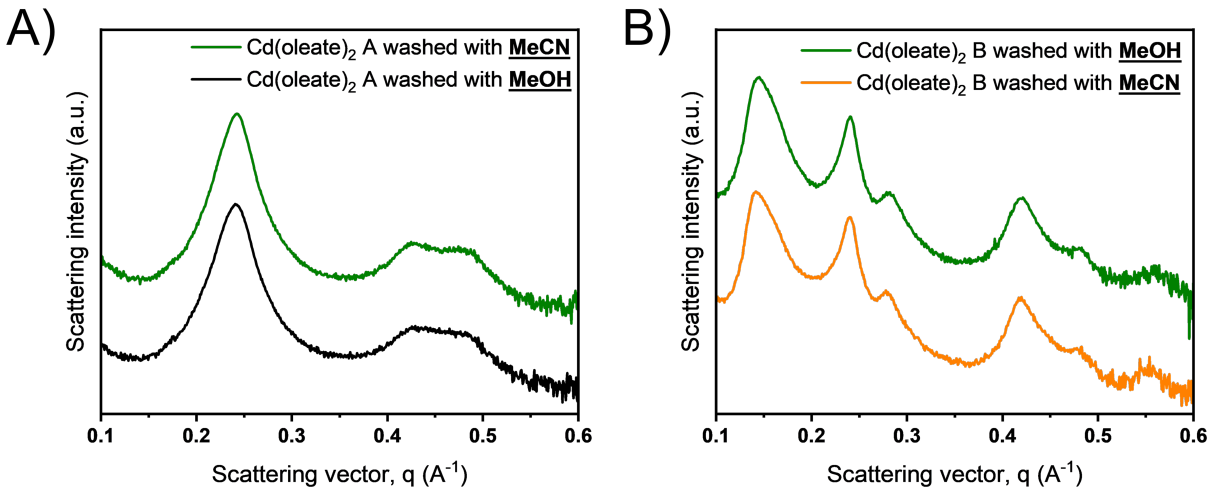

FIG. S23. SAXS patterns of $Cd(oleate)_2$ A) A and B) B washed with different washing procedure showing no effect of the nature of the solvent used on the structure of the Cd precursors.